Article

Structure

Two cooperative lipid binding sites within the pleckstrin homology domain are necessary for AKT binding and stabilization to the plasma membrane

Graphical abstract

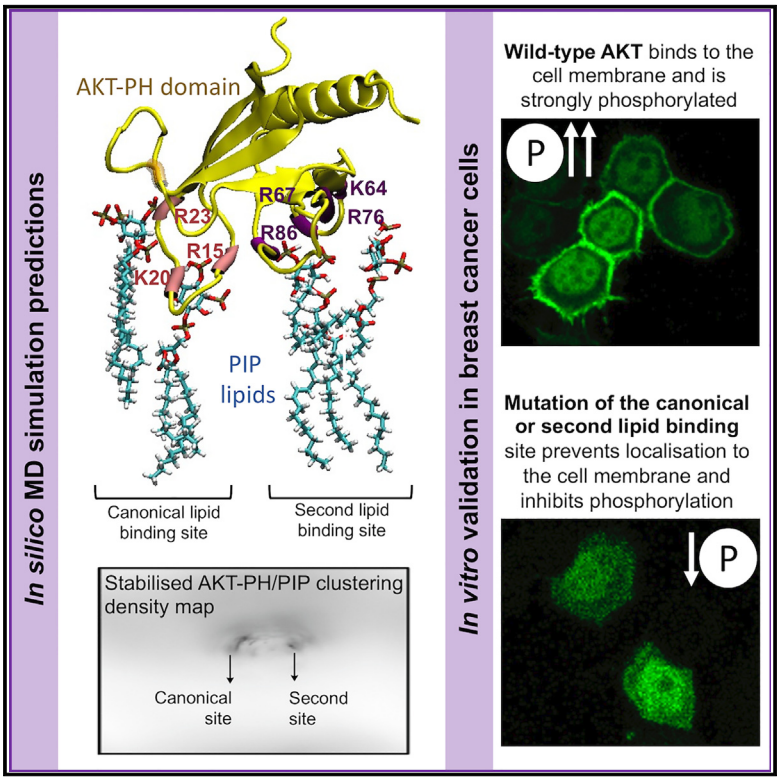

Highlights

- A second PIP binding site was identified in the AKT PH domain
- Both PIP binding sites are necessary for a stable orientation of AKT in the membrane
- Mutation of either PIP binding site stops AKT membrane localization and phosphorylation

Authors

Chrysa Soteriou, Mengfan Xu, Simon D. Connell, Arwen I.I. Tyler, Antreas C. Kalli, James L. Thorne

Correspondence

a.kalli@leeds.ac.uk (A.C.K.), j.l.thorne@leeds.ac.uk (J.L.T.)

In brief

Soteriou et al. identified a second PIP binding site in AKT's PH domain. When this second binding site is mutated, both membrane binding and phosphorylation of AKT were impaired. The existence of a second PIP binding site indicates there are additional mechanisms of AKT regulation that may have therapeutic potential.

Soteriou et al., 2025, Structure *33*, 181–195
January 2, 2025
https://doi.org/10.1016/j.str.2024.10.020

CellPress

Structure

CellPress
OPEN ACCESS

Article

Two cooperative lipid binding sites within the pleckstrin homology domain are necessary for AKT binding and stabilization to the plasma membrane

Chrysa Soteriou,[1,2,3] Mengfan Xu,[1] Simon D. Connell,[2,4] Arwen I.I. Tyler,[1] Antreas C. Kalli,[3,4,*] and James L. Thorne[1,5,*]
[1]School of Food Science and Nutrition, University of Leeds, Leeds LS2 9JT, UK
[2]Molecular and Nanoscale Physics Group, School of Physics and Astronomy, University of Leeds, Leeds LS2 9JT, UK
[3]Leeds Institute of Cardiovascular and Metabolic Medicine, School of Medicine, University of Leeds, Leeds LS2 9JT, UK
[4]Astbury Center for Structural Molecular Biology, University of Leeds, Leeds LS2 9JT, UK
[5]Lead contact
*Correspondence: a.kalli@leeds.ac.uk (A.C.K.), j.l.thorne@leeds.ac.uk (J.L.T.)
https://doi.org/10.1016/j.str.2024.10.020

SUMMARY

Almost four decades after the identification of the AKT protein and understanding of its role in cancer, barriers remain in the translation of AKT inhibitors for clinical applications. Here, we provide new molecular insight into the first step of AKT activation where AKT binds to the plasma membrane and its orientation is stabilized in a bilayer with lateral heterogeneity (L_o-L_d phase coexistence). We have applied molecular dynamic simulations and molecular and cell biology approaches, and demonstrate that AKT recruitment to the membrane requires a second binding site in the AKT pleckstrin homology (PH) domain that acts cooperatively with the known canonical binding site. Given the precision with which we have identified the protein-lipid interactions, the study offers new directions for AKT-targeted therapy and for testing small molecules to target these specific amino acid-PIP molecular bonds.

INTRODUCTION

The PI3K/AKT pathway is essential for normal cellular physiology. Hyperactivation of AKT, either via oncogenic transformation, expression, or activity of up or downstream pathway components[1,2] causes cells to divide more rapidly, evade apoptotic signaling[3] and is linked to drug resistance and worse survival rates for patients with breast and many other cancer types.[4] AKT is a peripheral membrane protein kept in an inactive conformation in the cytosol by interaction between the pleckstrin homology (PH) and kinase domains. Availability of membrane phosphatidylinositol-3,4-bisphosphate (PIP_2) and phosphatidylinositol-3,4,5-trisphosphate (PIP_3), referred to here as PIP lipids, determines AKT-PH/PIP binding and consequently kinase activity of the protein. PIP-AKT interaction leads to AKT phosphorylation at Thr-308 (central kinase domain)[5] and Ser-473 sites (C-terminal regulatory domain),[6] which are required for full AKT activity. Wild-type (the proto-oncogene form) AKT (AKT^{WT}) is active when bound to PIPs[7–9] and excess production of PI(3,4,5)P_3 results in increased activation of AKT,[7] leading to multiple cancer hallmarks.[10] Phosphorylated cytosolic AKT is short lived as membrane PIP availability is proportional to the AKT-activating stimulus,[7,11] indicating the importance of membrane lipids in AKT activation in cancer. Additionally, the more potent and higher activation of AKT and proteins upstream of the AKT pathway in cholesterol-rich liquid ordered (L_o) phases, compared to cholesterol-poor liquid disordered (L_d) regions of the membrane has been well reported.[12–17] Therefore, membrane lipids[18] and membrane cholesterol[12,13,19] have been a major target for attenuating AKT activity, and AKT has been a central target for cancer therapeutics.

Among peripheral membrane proteins, PH domains (100–200 amino acids long) are conserved at the structural level in terms of their three-dimensional organization but have low sequence homology.[20] PH domains consist of seven β strands that form two nearly orthogonal anti-parallel β sheets and one α helix in the C-terminal.[21] The first β sheet contains four anti-parallel β strands (β1–β4), and the second β sheet contains three anti-parallel β strands (β5–β7).[22] The primary binding site of most PH domains to PIPs is located between the β1-β2 and β3-β4 loops of the PH domain.[23,24] In some cases, PH domains bind PIPs on the opposite face of the β1-β2 loop, defined as non-canonical binding sites. Some examples of peripheral proteins with non-canonical binding sites include the ADP-ribosylation factor GTPase-activating protein (ArfGAP) with SH3 domain ankyrin repeat and PH domain 1 (ASAP1-PH),[25] Bruton's tyrosine kinase (BTK-PH),[26] and PH domain-containing family A member 7 (PLEKHA7-PH).[27] A canonical-binding site between positively charged residues in the β1-β2 loop and PIPs via electrostatic and hydrogen-bonded interactions[21,28,29] has been suggested for AKT-PH, with a few studies indicating some interactions of lipids outside this canonical-binding site.[24,30] However, it remains elusive how a non-canonical binding side on AKT-PH would affect its interaction and stabilization to membranes.

To identify how AKT is activated, previous studies have targeted specific amino acid residues within the AKT-PH and kinase domains,[21] deleted the entire PH domain,[7,21,31] or mutated residues at the PH-kinase domain interface.[32] X-ray crystallographic data have identified important PIP-interacting residues in the AKT-PH domain, but such studies are limited to 1:1 binding of AKT-PH to the PIP lipid head group.[28] Collectively these studies demonstrated that the region of the AKT-PH responsible for interacting with PIPs is primarily the basic patch between strands β1-β2 and the loop in between residues 13–23 and 53 of the PH domain.[24,28–30] However, the exact molecular requirements of AKT binding and orientation stabilization in a lipid environment with lateral heterogeneities remain unknown.

Here, we show with molecular dynamic prediction and *in vitro* validation that the first steps of AKT activation, specifically its membrane binding interface and stabilization with a phase separated bilayer, upstream of the dissociation of PH/kinase interface and all phosphorylation events of the protein, occur within two cooperative binding sites of the AKT-PH domain.

RESULTS

AKT-PH recruitment and stabilization to the membrane requires PIP lipids

The WT AKT-PH (AKT-PH^{WT}) domain (PDB-ID: 1UNQ)[28] was placed ∼7 nm away from a symmetric model membrane of lipids that resembles a phase-separated bilayer previously suggested to play a role upstream of the initiation of AKT pathway[14] and coarse-grained molecular dynamics (CG-MD) simulations were performed. Twenty repeats of the simulation were run in the absence (Figure 1A) and presence (Figure 1B) of PIP lipids. As expected, on average, AKT-PH^{WT} did not anchor to the lipid bilayer in the absence of PIPs (17/20) (Figure 1C), but in the presence of 10% PIPs, AKT-PH^{WT} diffuses in the aqueous environment and rapidly (<1μs) binds to the bilayer in all simulation repeats (20/20).

Lipid-lipid contact analysis showed that as time passes there is a lateral demixing of lipids into cholesterol-enriched L_o and cholesterol-scarce regions of L_d lipid phases (Figure S1). To ensure the lipid bilayer had already phase-separated at the time point of AKT-PH bilayer binding, radial distribution function (RDF) analysis of lipids were compared for the first μs (time point of AKT-PH binding), the last two μs (stabilized AKT-PH), and the average 7 μs of simulation time. The RDF of lipids (Figure S2A) and the visualization of simulation trajectories with protein (Figure S1A, snapshot of unbound protein bilayer), and without protein (Figures S2C and S2D) proved the formation of L_o/L_d domains within the first 1.5 μs of simulation time, indicating that phase separation had occurred prior the AKT-PH bilayer binding. RDFs of lipids further suggested that the incorporation of PIP lipids and/or AKT-PH domain into the model membranes did not affect the phase separation of lipids (Figure S3D). RDF analysis further showed high self-clustering between di-palmitoyl-phosphatidylcholine (DPPC) (marker for L_o phase) and di-linoleoyl-phosphatidyl-choline (DLiPC) lipids (marker for L_d phase), while low preference was observed for DPPC-DLiPC interactions (Figures S1A and S1B). Analysis for the PIP lipid preference for the DPPC-L_o or the DLiPC-L_d phase showed that PIPs had a greater probability of being surrounded by cholesterol and DPPC lipids compared to DLiPC lipids (Figure S1C). These results indicate the overall localization of PIP lipids in the L_o phases of the phase-separated bilayer. The AKT-PH domain are localized in close proximity to where PIP lipids are found in the L_o regions (Figure S1D).

The crystal structure of AKT-PH^{WT} (PDB 1D: 1UNQ)[28] bound to inositol (1,3,4,5)P4 (I4P) shows that I4P is in close proximity with several residues, including K14 (with 3,4-phosphates), R23 (with 1,3-phosphates), N53 (with 3,4-phosphates), and to a limited extent R86 (with 4-phosphates) of the AKT-PH^{WT} domain[28] (Figure 1D, upper structure in pop-out box). The CG simulations showed that the orientation and binding of PIP lipids closely resembled the crystal structure but identified additional residues that form a second binding site (Figure 1D, see bottom structure in pop-out box). Our simulations indicated AKT-PH^{WT} residues R23 and R86 were in contact with PIPs, which is in agreement with the crystal structure. In addition, K14 (crystal structure) was structurally close to R15 (simulated structure) (Figure 1D). The model also agreed with the crystal structure regarding residues K20 and R25, both of which had considerable PIP contacts in the simulated structure and were in close proximity to I4P in the crystal structure (Figure 1D). Further analysis of the PIP_3 lipid density distribution around the AKT-PH^{WT} indicated this clustering occurred around two binding sites of the AKT-PH^{WT} domain as soon as its orientation was stabilised at the membrane (5–7 μs) (Figure 1E). These data indicate that the simulation systems can replicate key features of physiological AKT-membrane binding and suggest that a second binding site is important for both the recruitment and stabilization of AKT-PH^{WT} to the bilayer.

The simulated AKT-PH^{WT}-PIP interaction occurs in an additional non-canonical binding site for AKT-PH

In order to establish the interaction of AKT-PH^{WT} with lipids, the protein-lipid contacts were calculated to identify residues contributing to AKT-PH^{WT} binding to the bilayer (binding+50 ns) and orientation stabilization to the bilayer (stabilization-7μs). Protein binding to the membrane is considered here when AKT-PH first interacts to the membrane (within a cut-off of 4.3 nm z axis = interaction) and protein orientation stabilization is considered when AKT-PH anchors to the membrane and maintains a specific stabilized orientation with membrane lipids (within a cut-off of 3.6 nm z axis = orientational stabilization). The simulations support the hypothesis that there are considerable contacts between PIPs and the β1-β2 loop (canonical binding site-gray shaded area) during binding with K20, R23 residues (Figure 2B), and at stabilization with R15, K20, and R23 residues (Figure 2B). K64, R67, R76, and R86 (β5–β7 strands) also made substantial contacts (AKT-PH^{WT}/PIP contacts >70% cut-off) with PIPs indicating these may be important residues for both binding and orientation stabilization of AKT-PH^{WT} to the bilayer (Figure 2B). The AKT-PH^{WT} bound PIPs with a similar orientation to the bilayer at the binding and the stabilization stage (Figure 2B, right 3D structures see residues in red).

With the aim of studying the protein stability, the final configuration of a CG trajectory was converted to an atomistic resolution and three simulation repeats were simulated for a further 100 ns using the CHARMM36 force field.[33,34] The root-mean-square deviation (RMSD) analysis in all our simulations ranged between

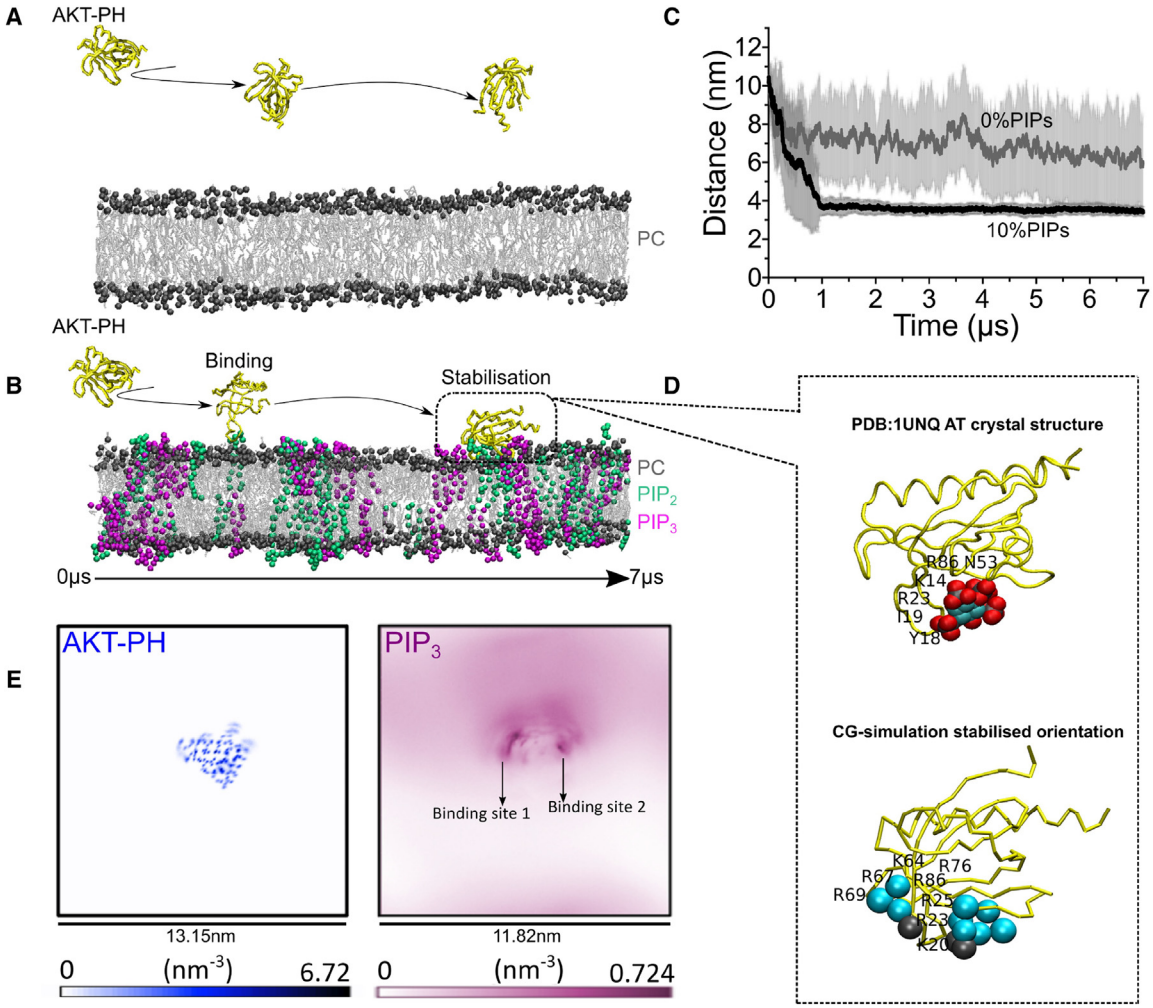

Figure 1. CG-MD model indicates anionic PIP lipids are required for the recruitment of AKT-PH^{WT} to the bilayer

(A and B) A simulation snapshot of AKT-PH binding and stabilising to the bilayer with (A) 0% PIP lipids (B) 5% PIP_2 lipids (green) and 5% PIP_3 lipids (magenta).

(C) Mean distances (solid line) ±SD (faded colors) between the center of mass of the AKT-PH domain and the lipid bilayer for the 20 × 7 μs simulations with (black) or without PIP (gray) lipids.

(D) AT crystal structure (PDB: 1UNQ) and the CG stabilised AKT-PH^{WT} (this paper) is shown to the right. The location of the amino acid residues that contact the bilayer the most is shown for both structures. Red = oxygen, cyan = carbon, gray = phosphates.

(E) Two-dimensional density maps of AKT-PH^{WT} (left) and PIP_3 lipids (right) in the x-y plane, with summation of density along the z axis. The right diagram shows average densities and the probability density of finding the PIP lipids at a given point in the bilayer plane around the carbon atoms of the protein (shown in the left diagram), color-coded with light pink representing low probability and dark pink representing high probability. The corresponding molecular model is shown in Figure 1D. Data are shown for the final 2 μs of a concatenated trajectory of all 20 simulation repeats for the control model membrane (5% PIP_2 and 5% PIP_3), showing the PIP_3 lipid distribution and clustering in two binding sites of AKT-PH^{WT}. Abbreviations: AKT-PH = Pleckstrin homology domain of AKT, AT = atomistic WT = wild type, CG = coarse-grained PIP = phosphatidylinositol, PIP_2 = phosphatidylinositol-3,4-bisphosphate, PIP_3 = phosphatidylinositol-3,4,5-trisphosphate, PDB = protein databank.

~0.3–0.4 nm over time, indicating that there were not any major protein conformational changes compared to the CG structure (Figure S4A). The root-mean-square fluctuation (RMSF) analysis also showed lower values in the structured regions of the protein, indicating that the AKT-PH is stable (Figure S4B). Protein-lipid contact analysis of our atomistic simulations revealed that residues R15, K20, R23 (canonical binding site), and residues K64, R67, R76, and R86 (proposed second binding site) form the larger number of interactions with the phosphates of the PIP lipids, being in agreement with our CG systems (Figure 3A). Additionally, residues R41 and R48, which lie within the β3-β4 strands of the AKT-PH domain, made considerable contacts with PIPs in the atomistic simulations (Figure 3A), which were not as evident in the CG-systems (Figure 2). The PIP interaction of residues in the β3-β4 strands (such as N53) has been previously suggested[28] and is likely subsequent to PIP interactions with the canonical binding site of the protein. Precisely, some residues in the β3-β4 strands of AKT-PH, such as R41 and R48 lie in a very close proximity to residue R23 (Figure 3B), which is one of the key known canonical binding pocket residues in the crystal structure[28,29] and in our CG simulations (Figure 2). Nonetheless, the atomistic AKT-PH maintains the same orientation seen in the

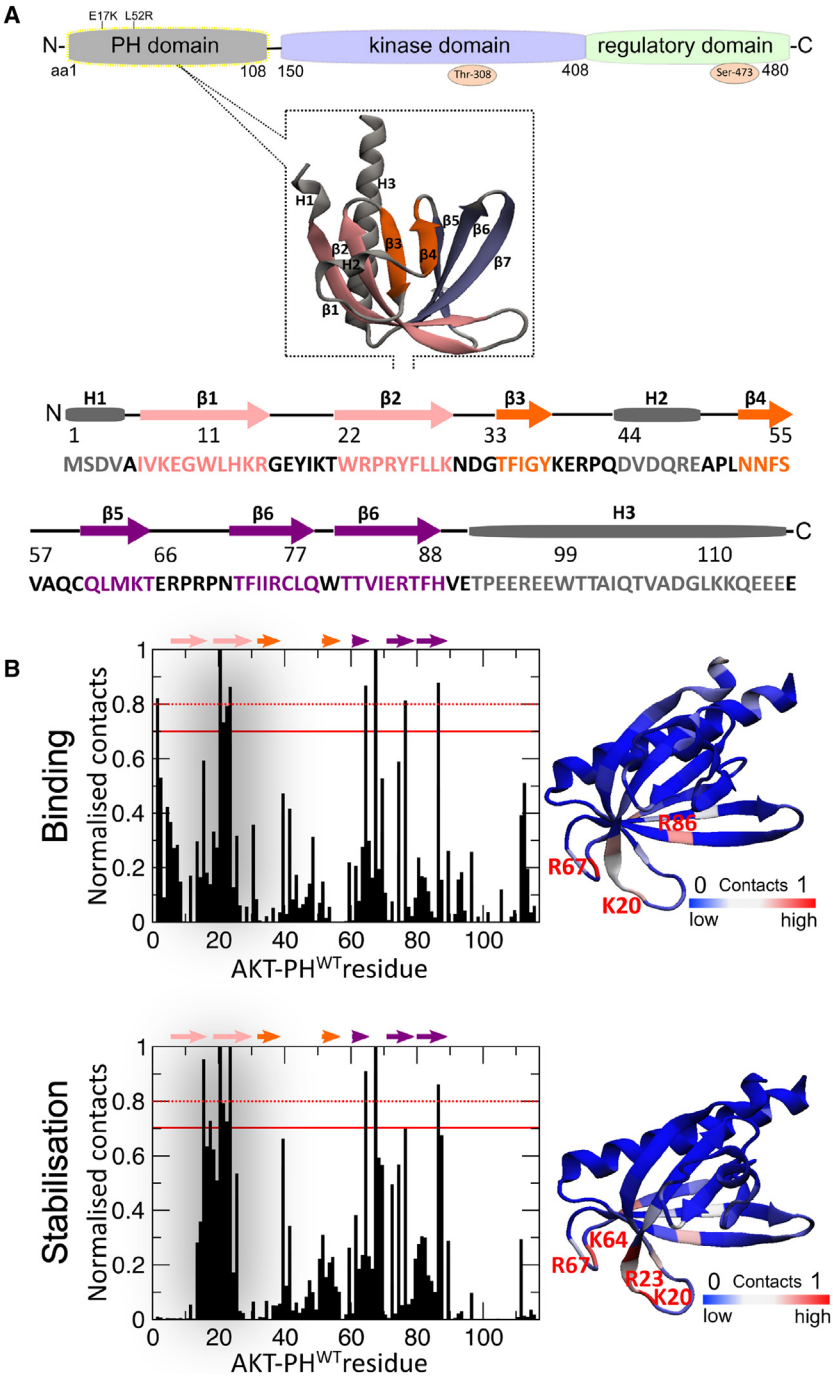

Figure 2. AKT-PH^{WT} interactions with PIPs occur via two binding sites

(A) The domains of full-length WT AKT and a zoomed image of the AKT-PH domain with beta strands and helixes labeled. The primary and secondary structure of the AKT-PH domain color coded for each beta-strand. AKT-PH consists of seven β-strands that form two nearly orthogonal anti-parallel β sheets and one α helix in the C-terminal. The first β sheet contains four anti-parallel β strands (β1–β4), and the second β sheet contains three anti-parallel β strands (β5–β7).

(B) Shown are normalized contacts between AKT-PH^{WT} and PIP headgroups during the binding of AKT-PH^{WT} to the bilayer (top) or stabilization (bottom). Normalization was performed by dividing the total number of contacts at each residue by the total contacts made by the residue with the highest number of contacts in the AKT-PH^{WT} domain. Red solid lines represent the cut-off of 70% of the contacts and are considered to be the most important residues for electrostatic interaction with PIPs. An upper cut-off of 80% of the contacts is shown in dotted red lines. The gray-shaded area shows the known canonical-binding site. The position of the β1 and β2 strands (pink), β3 and β4 strands (orange) and β5-β7 strands (purple) are shown by the arrows. To the right of each histogram is the structure of AKT-PH^{WT} domain color coded based on the number of contacts with PIP_3 lipids during binding and stabilization. Blue indicates 0 contacts and red indicates high number of contacts above the 70% cut-off. Abbreviations: AKT-PH = Pleckstrin homology domain of AKT, PIP = phosphatidylinositol, PIP_3 = phosphatidylinositol-3,4,5-trisphosphate, WT = wild type.

CG-systems, where multiple PIP lipids bind to two-binding sites of the AKT-PH domain (Figure 3C). These data indicate that K64, R67, R69, and R76, form a second PIP binding site in addition to the previously reported AKT-PH^{WT} binding site.

Mutations of key AKT-PH residues propagate orientational changes to attenuate protein orientational stability of AKT-PH to the bilayer

Following the discovery of an additional PIP binding site for the AKT-PH^{WT} domain, *in silico* mutations were performed to explore each site's relative and combined contribution to membrane binding and orientation stabilization. The most critical amino acids in terms of contacts and charge (according to Figures 2B and 3A) were a series of arginine and lysine residues and these were swapped for the non-charged alanine and are thus unable to interact with PIP lipids. Three mutation simulations were, therefore, made that simulate the loss of positive charge of the canonical (AKT-PH^{mut1}), second (AKT-PH^{mut2}), or both canonical and second PIP binding sites (AKT-PH^{mut3}) (Figure 4A). AKT-PH^{mut1} had four mutations, all within the β1-β2 strands, and AKT-PH^{mut2} had five mutations spread across the antiparallel three-stranded β5, β6, and β7 sheet. AKT-PH^{mut3} combined all the mutations of AKT-PH^{mut1} and AKT-PH^{mut2}, as described previously (Table 1).

Even-though the simulation repeats of all systems tested eventually resulted in AKT-PH-membrane associations, the AKT mutants displayed a less stable membrane association versus the WT, as seen by the greater standard deviation of the mean distance between the AKT-PH and the bilayer. Therefore, the mutations did not affect the binding frequency of the AKT-PH but strongly affected the orientation of AKT-PH during

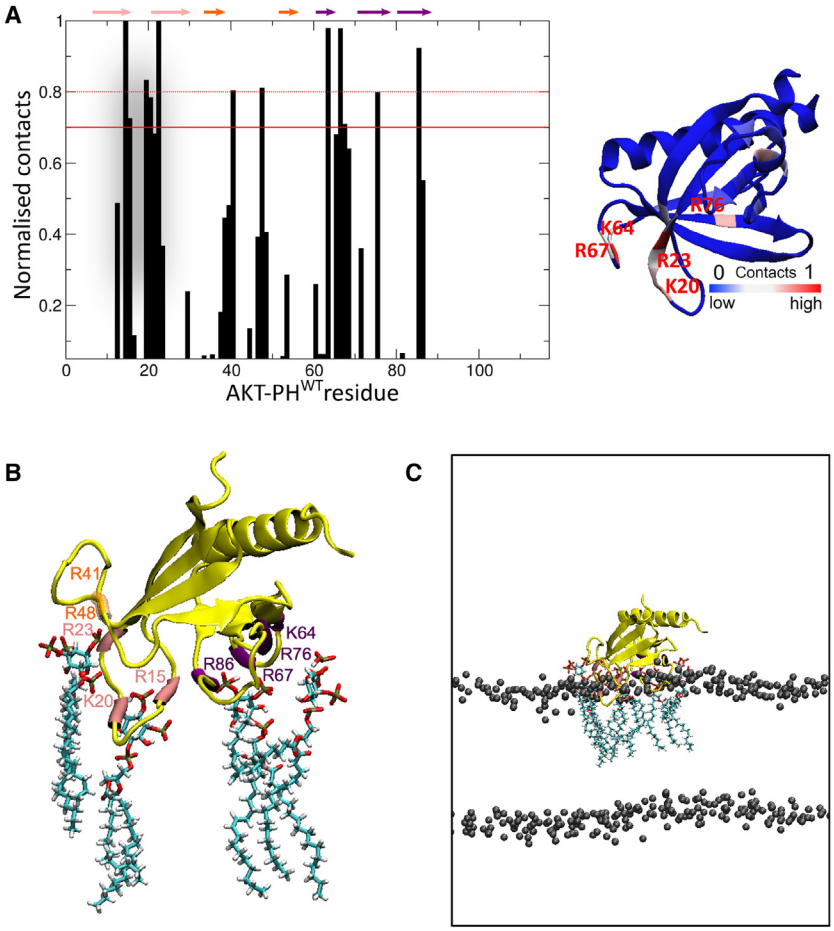

Figure 3. An atomistic model of our system showing AKT-PH^{WT}/PIP interactions via two binding sites

(A) Normalized contacts between AKT-PH^{WT} and PIP headgroups after 100 ns of atomistic simulations. Normalization was performed by dividing the total number of contacts at each residue by the total contacts made by the residue with the highest number of contacts in the AKT-PH^{WT} domain. The dotted red line represents the upper cut-off of 80% of the contacts and is considered to be the most important residues for electrostatic interaction with PIPs in the higher-resolution atomistic system. The solid red line represents the cut-off of 70% of the contacts, which was used in the CG-systems and is considered to form considerable contacts with the PIP lipids. The gray-shaded area shows the known canonical-binding site. The position of the β1 and β2 strands (pink), β3 and β4 strands (orange), and β5–β7 strands (purple) are shown by the arrows. To the right of the histogram is the structure of the backmapped AKT-PH^{WT} domain color coded based on the number of contacts with PIP_3 lipids. Blue indicates 0 contacts and red indicates high number of contacts above the 80% cut-off.

(B) Snapshot of the stabilised orientation of the atomistic AKT-PH^{WT} structure showing that the interactions of the canonical and second AKT-PH binding sites are retained in the atomistic model, with the interacting residues with PIPs shown.

(C) The atomistic AKT-PH^{WT} maintains the same orientation seen in the CG-systems, where multiple PIP lipids bind to two-binding sites of the AKT-PH domain. The phosphate atoms of DPPC and DLiPC lipids are shown in gray. Abbreviations: AKT-PH = pleckstrin homology domain of AKT, PIP = phosphatidylinositol, PIP_3 = phosphatidylinositol-3,4,5-trisphosphate, WT = wild type.

stabilization to the bilayer (Figure 4B). Additionally, all mutants showed reduced clustering with PIPs compared to AKT-PH^{WT} throughout the 7 μs of simulation time (Figure 4C). These observations prompted us to investigate the effect of the AKT mutants on the protein's orientational changes.

In order to quantitatively study the orientational changes that could affect the orientational stability of AKT-PH^{WT} and mutants, the angle theta between the bilayer z axis and a plane defined by three amino acid residues (94, 102, and 108) of AKT-PH (in structured regions of the protein) was measured over all simulation frames (Figure S5). This analysis allows for studying the populations of the protein's preferred orientation when unbound (blue = reduced density) or bound to the membrane (red = greater density) (Figure 4D). WT and mutated AKT-PH diffused freely in solution before interacting with the bilayer at approximately 4.3 nm (cut-off for protein binding, Figure 4D). AKT-PH^{WT} adopted a preferred membrane-bound orientation with theta between 130 and 170° (productive state of AKT-PH) and a small population of an alternative lowly populated membrane-bound state (angle theta between 100 and 120°) (Figure 4D, top histogram). The productive state of AKT-PH is a state in which the two identified lipid-binding sites are facing the bilayer, as seen in simulations of the WT protein (Figure 1). As expected, the productive state of AKT-PH^{WT}, which is believed to be the most relevant state to the function of the protein, was more populated during stabilization than at binding (Figure S6).

AKT-PH^{mut1} and AKT-PH^{mut2} also bound the bilayer with the productive state (theta 130–170°), although they also explored new orientations that spread between 25 and 125° during binding and stabilization (Figure 4D, middle histograms). AKT-PH^{mut3} spent more time in solution (more unbound states shown in purple; Figure 4D, bottom histogram) but mostly completely changed its orientation to the bilayer compared to AKT-PH^{WT}, diminishing the protein's productive orientation state (Figures 4D and S6). Therefore, the mutants overall did not affect the ability of the protein to bind the bilayer but rather the bound protein explored more (non-productive) orientation states compared to AKT-PH^{WT}, being more orientationally unstable than AKT-PH^{WT}.

The next step was to understand the impact of the mutations on AKT-PH's ability to interact with PIPs. Therefore, protein-PIP contact analysis was performed. The orientation of all three mutated AKT-PH domains (based on their PIP-binding residues >70% cut-off) was different compared to AKT-PH^{WT} during both binding and stabilization (Figure 4E). In agreement with the orientation analysis (Figure 4D), there was a wider distribution of positions that interacted with PIPs in the mutated systems compared to AKT-PH^{WT}; however, AKT-PH^{mut2} and AKT-PH^{mut3} still maintained considerable wild-type binding than AKT-PH^{mut3} (Figure 4E). AKT-PH^{mut1}

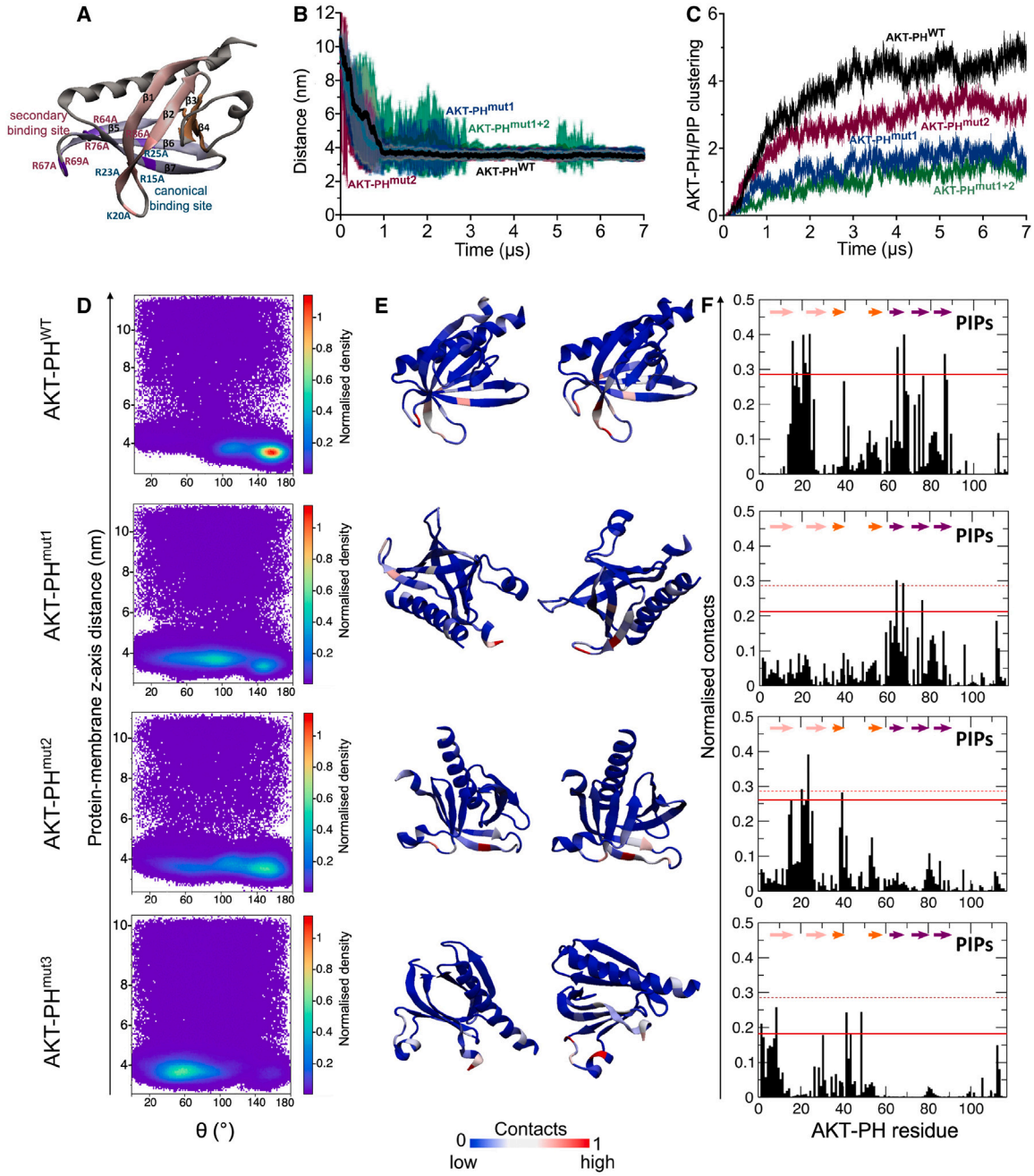

Figure 4. Mutations of key binding/stabilising AKT-PH residues propagate orientational changes to diminish AKT-PH's productive orientation state

(A) Position of β strands and mutants within the AKT-PH domain.

(B) Mean distances (solid line) ±SD (faded colors) between the center of mass of WT and mutant AKT-PH domain and the lipid bilayer.

(C) Mean number of the PO4 (CG representation of position 1 phosphate particles) of PIP lipids contacting the AKT-PH as a group within 0.6 nm per simulation time.

(D) Two-dimensional histograms showing the average density states observed on a grid of AKT-PH-membrane z-distance and protein orientation (angle theta) for AKT-PH^{WT}, AKT-PH^{mut1}, AKT-PH^{mut2} and AKT-PH^{mut3}.

(E) The structure of AKT-PH^{WT} and mutated AKT-PH domain color-coded based on the number of contacts with PIP_3 headgroups during binding and stabilisation. Blue = 0 contacts, and red indicates high number of contacts above the 70% cut-off (F) The normalized average number of contacts between the AKT-PH protein and PIP headgroups for each system during stabilization. Normalization was done by dividing the number of PIP lipids and the total number of frames

(legend continued on next page)

bound to the bilayer (via PIP interactions) with residues M1, K64, R67, and R76 and stabilized to the bilayer with residues K64, R67, and R76 (Figure 4F). This analysis shows that eliminating the positive charge in AKT-PH's canonical PIP-binding site (AKT-PH^{mut1}) allows its binding and stabilization to occur with residues in the β5-β7 strands (second binding site) (Figure 4F). Mutant AKT-PH^{mut2} bound the PIPs with residues R23 and R41 and stabilized in the bilayer with residues R15, K20, R23, and K39, with PIPs. Therefore, when the positive charge in AKT-PH's second binding site is eliminated (AKT-PH^{mut2}), bilayer binding and stabilization still occurs with residues in the β1-β2 strands (canonical binding site) (Figure 4F). The AKT-PH^{mut3} mutant bound PIPs with residues M1, S2 and was stabilized to the bilayer with residues M1, R48, R41, and Q43, completely altering and reducing AKT-PIP interaction compared to AKT-PH^{WT} (Figure 4F). This shows that eliminating the positive charge in both the canonical and second binding sites of AKT-PH compromises AKT-PH-PIP membrane binding and stabilization as the lipid-binding domains that interact with PIP lipids are unavailable (Figure 4F).

In summary, we concluded that the PIP binding region of the AKT-PH domain occurs in multiple binding sites and contacts from the β1-2 strands region are required in addition to the β5, β6, and β7 region described here. Both canonical and second regions are required for the long-lived (on the μs scale of MD simulations) association of AKT-PH with PIPs in the bilayer. To validate this, *in vitro* mutation experiments were performed to evaluate if changes to these amino acid residues could reduce membrane localization in cancer cell membranes.

The cooperative interaction of two AKT-PH/PIP binding sites *in vitro* in cancer cells

The *in silico* CG-MD simulations provided predictions that were testable *in vitro*. For example, CG-MD simulations suggested that mutations, which disrupted amino acid positive charge within the canonical or second AKT-PH/PIP binding sites, would propagate orientational changes to diminish AKT-PH's productive orientation state and reduce protein localization to the membrane (Figures 4D–4F). Specifically, we set out to ask if either or both AKT-PH/PIP binding sites were necessary and sufficient for membrane localization in triple-negative breast cancer (TNBC) cells, hence AKT-PH domain mutants were cloned into overexpression plasmids (Table 2).

To compare WT and mutated AKT protein behavior, the full-length AKT^{WT} was paired with the full-length AKT mutant proteins within a cell that eliminate the positive charge in the canonical (AKT^{mut1}), second (AKT^{mut2}), or both canonical and second PIP binding sites (AKT^{mut3}). As expected, when the red and green wild-type AKTs were co-transfected (AKT^{WT}-mCherry and AKT^{WT}-EGFP) they were equally localized to the membrane (Figure 5A, nested t test; $p > 0.05$). The pathogenic AKT^{E17K} mutant, known to enhance AKT translocation to the plasma membrane and protein activation,[35] was significantly more localized to the membrane than AKT^{WT} (Figure 5B, nested t test; p=0.0017). Localization of all three AKT-PH/PIP domain mutants to the plasma membrane was significantly attenuated relative to AKT^{WT} (Figures 5C–5E, nested t test; AKT^{mut1}: $p < 0.0001$; AKT^{mut2}: $p < 0.0001$; AKT^{mut3} $p = 0.0003$). Similarly, a significantly reduced membrane to cytosol fluorescence intensity ratio was observed in the mCherry-tagged AKT-PH^{mut3} mutant compared to its co-transfected EGFP-tagged AKT^{WT} (Figure S7, nested t test; $p < 0.0001$), indicating that the AKT mutants have similar membrane localization when the mutant is EGFP or mCherry tagged as well as when just the PH-domain or full-length AKT is over-expressed.

The similar expression of mCherry-fused AKT^{WT} (one-way ANOVA; $p > 0.05$, Figure S8) in each co-transfection experiment confirmed that the mutants (EGFP fused) could be compared, to determine if mutations in each binding site (canonical-AKT^{mut1}, second-AKT^{mut2}) or both (AKT^{mut3}) similarly affected AKT membrane translocation. There was no difference in the ability of AKT^{mut1}, AKT^{mut2}, or AKT^{mut3} to attenuate the AKT membrane translocation (Figure S9, one-way ANOVA; $p > 0.05$). The similar capacity to attenuate AKT membrane translocation in the three mutants indicates a cooperative action of the two binding sites in TNBC cells. Specifically, both binding sites (canonical and second) are required for normal AKT membrane localization (as in AKT^{WT}). Furthermore, targeting both binding sites (both canonical and second-AKT^{mut3}) did not exacerbate the attenuation of AKT membrane localization, again indicating the cooperative action of the two AKT-PH binding sites in TNBC cells.

The next step was to understand whether the mutations affect the downstream AKT activity at the cellular level by testing the phosphorylation levels of AKT$^{mut1\text{-}3}$ and their ability to attenuate AKT phosphorylation compared to the AKT^{WT}. We firstly treated TNBC cells with Perifosine, an AKT inhibitor which interferes with phospholipid metabolism and perturbs the membrane translocation of AKT,[36] as a negative control in order to identify and differentiate the endogenous and EGFP-tagged constructs, which as expected significantly repressed the phosphorylation of EGFP-AKT^{WT} (Figure 6A; t test; p=0.0009). As expected, the pathogenic EGFP-AKT^{E17K}, which facilitates membrane localization and phosphorylation of AKT in the absence or presence of growth factor stimulation,[35] showed significantly increased phosphorylation compared to EGFP-AKT^{WT} (Figure 6B, one-way ANOVA; $p < 0.0001$). Finally, the phosphorylation of all three mutants (EGFP-AKT$^{mut1\text{-}3}$) was significantly reduced relative to EGFP-AKT^{WT} (Figure 6B, one-way ANOVA; EGFP-AKT^{mut1}: p = 0.0021; EGFP-AKT^{mut2}: p = 0.0033; EGFP-AKT^{mut3}: p = 0.0019).

In conclusion, *in vitro* validation of the CG-MD simulation predictions in TNBC cells showed that one of the two identified binding sites (known canonical and second site) is insufficient for normal AKT membrane localization. Instead, the known canonical and second binding sites act cooperatively and are both required for AKT translocation to the membrane, which is the first step in its activation and subsequently for functional AKT activity as shown by phosphorylation.

analyzed. Solid red lines represent the cut-off of 70% of the contacts for each system and are considered to be the most important residues for electrostatic interaction with PIPs for each system. Red dotted line represents the original threshold line of the WT system indicating reduced PIP contacts of mutants. Data are shown as averages for the 20 × 7 μs simulation repeats/system. The position of the β1 and β2 strands (pink), β3 and β4 strands (orange) and β5- β7 strands (purple) are shown by the arrows (Abbreviations: PH = pleckstrin homology, PIP = phosphatidylinositol, WT = wild type.

Table 1. AKT-PH mutation list

AKT model	Point mutations to remove positive charge	β-strand affected
Point mutants informed from CG-MD		
AKT-PH^{mut1}	R15A	β1-β2
	K20A	β1-β2
	R23A	β1-β2
	R25A	β1-β2
AKT-PH^{mut2}	R64A	β5-β6-β7
	R67A	β5-β6-β7
	R69A	β5-β6-β7
	R76A	β5-β6-β7
	R86A	β5-β6-β7
AKT-PH^{mut3}	R15A	β1-β2
	K20A	β1-β2
	R23A	β1-β2
	R25A	β1-β2
	R64A	β5-β6-β7
	R67A	β5-β6-β7
	R69A	β5-β6-β7
	R76A	β5-β6-β7
	R86A	β5-β6-β7

DISCUSSION

Using *in silico* CG-MD and atomistic simulation prediction and *in vitro* validation in cancer cells, we studied the molecular insights of protein-lipid interactions of AKT in a bilayer entailing lateral heterogeneity. We identified the AKT-PH domain has two cooperative PIP-binding sites (previously known canonical and an additional second site). Targeting either or both binding sites attenuates AKT membrane localization and activation in TNBC cells.

X-ray crystallographic studies of AKT-PH provided valuable insights regarding the interaction of the protein to the head group of PIP_2 (IP3) or PIP_3 (IP4) lipids via the canonical binding site across the PH family.[28] However, X-ray crystallographic data only provide a 1:1 binding of the AKT-PH/PIP lipid head group.[28] CG-MD simulations, providing molecular context, allowed us to study the situation of having more than one PIP lipid in the bilayer and over time to understand the mechanistic details of protein-lipid associations during binding and orientational stabilization changes of AKT-PH.

CG-MD simulations showed the necessary presence of anionic PIP lipids for binding AKT-PH to a phase-separated model membrane (Figure 1). It was previously shown experimentally that the AKT/PIP_3 engagement allows phosphorylated AKT to be stable, promotes substrate engagement and protects AKT from dephosphorylation by cytosolic phosphatases.[7,11] As long as the AKT was bound to membrane PIP_3 lipids and was phosphorylated, it could also phosphorylate downstream substrates.[7] Contrary, if PIP_3 lipids were unavailable, AKT was inactive and dephosphorylated.[7] In our study, once the simulated AKT-PH^{WT} bound to the membrane, it maintained a stabilized orientation until the end of the 7 μs studied here (Figure 1C), but when PIPs were unavailable, AKT-PH neither bound nor stabilized to the bilayer, in agreement with previously published experimental data.[7,8]

The CG-MD simulations in this paper mimic a simple model of cholesterol-enriched lateral assemblies. Such cholesterol-rich lateral membrane assemblies have been known to form a platform for initiating AKT signaling cascades at the plasma membrane.[13,16,17,37] Direct comparison of AKT kinetics in living cells,[17] model membranes, live-cell isolated membranes (GPMVs) and fixed cells[12,14–17,38–40] showed L_o-membrane domain resident AKT to be activated more potently and the AKT phosphorylation to be more sensitive to cholesterol depletion than in L_d-membrane domain or cytosolic-resident AKT.[12,13,19,39] Therefore, previous research suggested that AKT is spatially involved with membrane lipid phases, with cholesterol guiding AKT activity. While not the main scope of this work, our simulations showed an association of PIPs and AKT with cholesterol-rich L_o phases, being in agreement with previous studies.[41–46]

In silico, we identified the known canonical binding site of AKT-PH^{WT} for PIPs (β1-β2 region), as well as an additional binding site located between β5-β7 strands of the PH domain (Figure 2A). Backmapping of our CG systems to atomistic simulations showed that the reported interactions of AKT-PH with PIP lipids were retained (Figure 3). In agreement with previous studies, we demonstrate that multiple PIPs are required to stabilize the orientation of AKT-PH to the bilayer (Figure 4C). Particularly, our CG-MD simulation model agrees with previous NMR data,[29] which showed that chemical shift changes in the binding of PIP_3 to AKT ceased at 4:1 PIP_3: AKT, potentially indicating the clustering of four PIPs around AKT (Figures 3C and 4C). Other PIP binding PH-containing peripheral proteins, like PLEKHA7, had multivalent binding with PIPs and induced PIP clustering as shown experimentally[27] and *in silico*.[24] A systematic simulation of 100 PH-containing proteins showed that PIP clustering might be occurring in the majority of the PH family.[24] The same study also concluded that AKT-PH has a similar PIP_2 non-canonical interaction site as seen in the Rho GTPase-activating protein 9 (ARHGAP9) PH domain[47] with the β5-β6 loop of AKT-PH.[24] Furthermore, Yamamoto et al. showed more than 60% of their simulation repeats to have a canonical binding of the AKT-PH/PIP complex but also noticed a few simulation repeats to occur in additional non-canonical binding sites.[30] It was suggested that these second binding sites might correspond to transient interactions prior to protein stabilization.[30]

Previous studies suggested that cytosolic AKT is very short-lived, and phosphorylated AKT is mainly connected with cellular membranes.[7,11] As with other peripheral proteins involved in cancer signaling, like ASAP1, multiple binding sites in the PH domain could keep such orientation to allow its downstream interaction with their protein targets.[48] One such target for AKT-PH is the 3-phosphoinositide-dependent kinase (PDK1) peripheral protein, which phosphorylates AKT and also has a PH domain.[5] The two cooperative binding sites in the ASAP1-PH domain were proposed to allow rapid switching between active and inactive states during signaling.[25] The proposed mechanism for ASAP1-PH could be a generalized mechanism for other PH domains with multiple cooperative binding sites, which remains an area for future research.[25] Additionally, multiple PIP binding with AKT-PH is a potential mechanism to slow the diffusivity of the protein, subsequently functionally allowing its stable orientation at the lipid bilayer. Mutating PIP-binding residues in the

Table 2. Plasmid construct mutation list

Construct	Mutation	PH location	Full length (FL)/PH only	Fluorescence tag
WT constructs				
AKT^{WT}-mCherry	–	N/A	FL	mCherry
AKT^{WT}-EGFP	–	N/A	FL	EGFP
Pathogenic mutants				
AKT^{E17K}-EGFP	E17K	β1-β2	FL	EGFP
Mutants informed from CG-MD				
AKT^{mut1}-EGFP	R15A	β1-β2	FL	EGFP
	K20A	β1-β2		
	R23A	β1-β2		
	R25A	β1-β2		
AKT^{mut2}-EGFP	R64A	β5-β6-β7	FL	EGFP
	R67A	β5-β6-β7		
	R69A	β5-β6-β7		
	R76A	β5-β6-β7		
	R86A	β5-β6-β7		
AKT^{mut3}-EGFP	R15A	β1-β2	FL	EGFP
	K20A	β1-β2		
	R23A	β1-β2		
	R25A	β1-β2		
	R64A	β5-β6-β7		
	R67A	β5-β6-β7		
	R69A	β5-β6-β7		
	R76A	β5-β6-β7		
	R86A	β5-β6-β7		
AKT-PH^{mut3}-mCherry	R15A	β1-β2	PH	mCherry
	K20A	β1-β2		
	R23A	β1-β2		
	R25A	β1-β2		
	R64A	β5-β6-β7		
	R67A	β5-β6-β7		
	R69A	β5-β6-β7		
	R76A	β5-β6-β7		
	R86A	β5-β6-β7		

known canonical and/or newly identified AKT-PH domain binding site might be adequate for AKT-PH membrane recruitment but compromises productive membrane-orientation stabilization (Figure 4E). A limited PIP availability in the two binding sites of AKT-PH would compromise the protein's functionality, in terms of being stably available for maintaining an active stimulus and interacting with its downstream targets.

Crystal structures of AKT in complex with allosteric inhibitors demonstrated that the autoinhibitory interface of AKT PH/kinase interaction occurs between residues F55, L52R, Q79K, W80, and T81 of the PH domain and residues T195, L321, and D325 of the kinase domain.[11,32,49] Based on these crystal structures, the residues that form the canonical and second binding sites of AKT with PIPs do not participate in PH/kinase interaction (Figure S10). However, one of the most recent studies that developed a crystal structure of autoinhibited AKT in the absence of allosteric inhibitors identified considerably different PH/kinase interacting residues than previous studies.[8] Truebestein et al. suggested that residues in the known PIP/AKT-PH canonical binding site interact with kinase residues to autoinhibit AKT.[8] Besides, recent evidence demonstrated that R86A mutation (part of the second binding site identified here) on the AKT-PH domain showed increased PH/kinase affinity, subsequently increasing autoinhibition of AKT activity.[50] Still, it is widely accepted that the activity of AKT strongly depends on the availability of PIP lipid signals preceding kinase activity and AKT phosphorylation.[7,8,11]

Our study supports the notion of decreased AKT activity following R86A mutation, as it forms part of the newly identified binding site to PIP lipids. Therefore, we suggest and have validated experimentally (Figure 6B) that in the event of unavailability of residues in the canonical and second binding sites of AKT-PH domain to bind PIPs, the AKT-PH will likely be inactive, and therefore PH/kinase domain interaction (inactive AKT state) will be expected. The order of events in the activation of AKT would be as such, the PIP activating stimulus results in the recruitment of AKT-PH via its two binding sites to the membrane and subsequently, the unmasking of the AKT's kinase domain for phosphorylation by PDK1[28] and mammalian target of rapamycin complex 2 (mTORC2).[51] Future studies should identify if all AKT-PH residues that form the two binding sites with PIPs identified here, show an increase of autoinhibitory features through enhancement of PH/kinase intramolecular interaction.

PH domain-PIP complexes can be selectively targeted by small molecule inhibitors for anti-cancer therapeutic manipulation, as

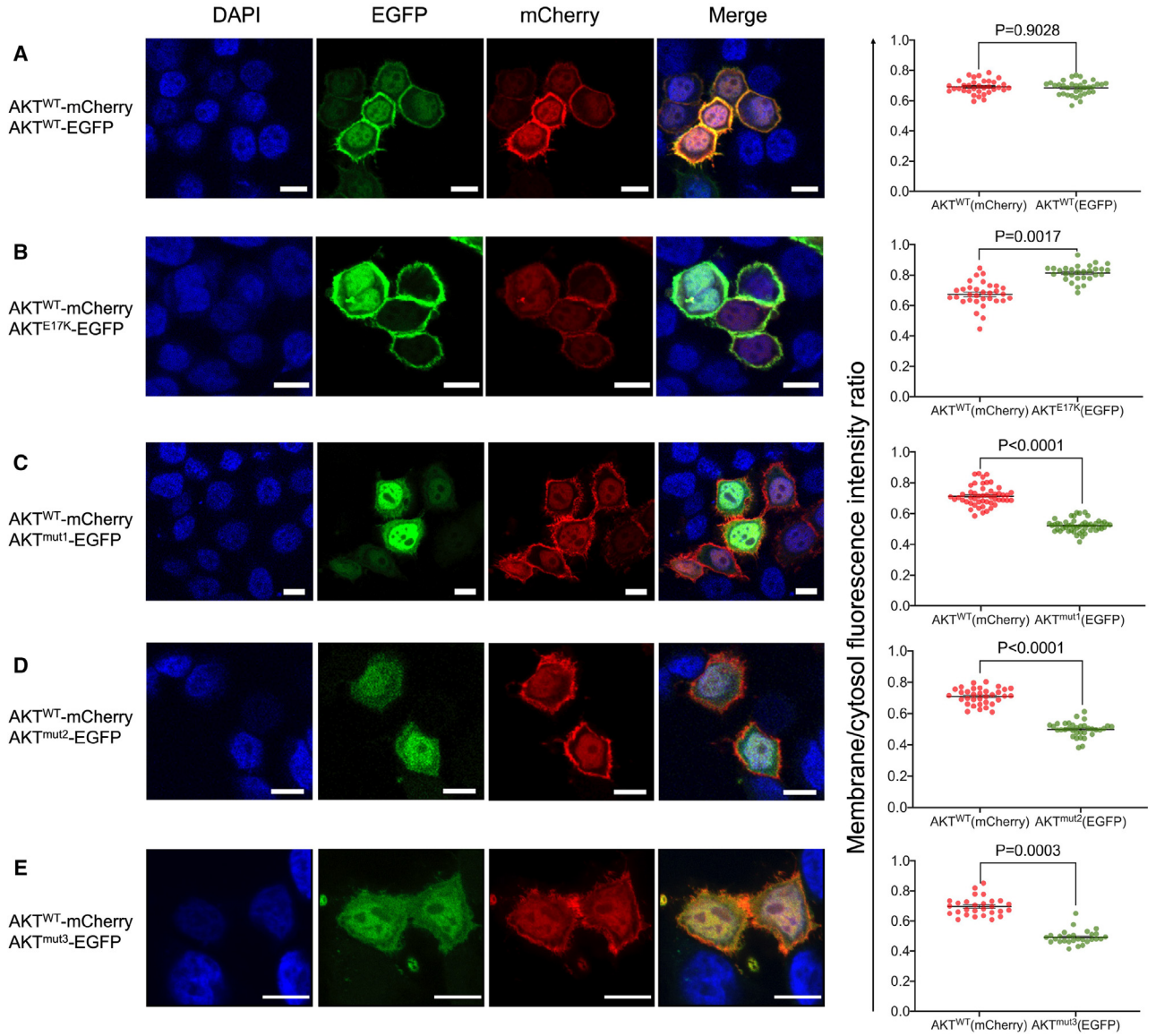

Figure 5. Mutations in the canonical and second binding sites attenuate AKT membrane localization in untreated TNBC cells

Representative confocal images showing co-expression of AKT^{WT} (mCherry) with AKT-EGFP (A) AKT^{WT} (B) AKT^{E17K} (C) AKT^{mut1}, (D) AKT^{mut2}, (E) AKT^{mut3} in MDA-MB-468 TNBC cells. Scale bars represent 10 μm. For each confocal image, DAPI staining, EGFP, and mCherry signal is shown independently and as a merged image. A quantitative nested analysis showing the biological and technical replicates (multiple cells per confocal image) for each co-transfection is shown to the right of every image. Data are represented as mean and SEM from four biological replicates with a total of (A) $n = 85$, (B) $n = 82$ (C) $n = 109$, (D) $n = 81$, (E) $n = 35$ quantified. Statistical analysis was performed with a two-tailed nested t-test between the AKT^{WT} and the mutants. $p \leq 0.05$ was considered significant. Abbreviations: EGFP = enhanced green fluorescence protein, TNBC = triple-negative breast cancer, WT = wild type.

was shown for the PH domains of PIP_3 dependent Rac exchanger (P-Rex1)[52] and brefeldin A-resistant ArfGEF 2 (BRAG2).[53] A few AKT-PH inhibitors have also been designed for therapeutic interventions at the membrane binding of the PH domain of AKT.[18,54,55] Triciribine, for example, targets residues in the canonical binding site of AKT that contact the D3-phosphate of PIP_3, such as K14, R23, R25, and N53.[18] To date, despite extensive research on AKT only a single AKT inhibitor has reached Food and Drug Administration (FDA) but not European Medicines Agency (EMA) approval.[56] Capivasertib has been very recently approved by the FDA, for the treatment of hormone receptor positive human epidermal growth factor 2 (HER2)- negative breast cancer with one or more AKT alterations.[56] Still, none of the AKT inhibitors has been positive in phase III trials[57] with TNBC as an indication, and the design of AKT-targeted therapies remains an active field of research.[58]

To conclude, we studied the molecular details of the AKT-PH/PIP interaction to identify and validate its PIP-binding sites in a phase-separated bilayer model. The findings demonstrated that AKT is an additional case of a PH-containing peripheral protein with multiple binding sites, similar to ASAP1-PH,[25] BTK-PH,[26] and PLEKHA7-PH.[27] Two cooperative binding sites (the

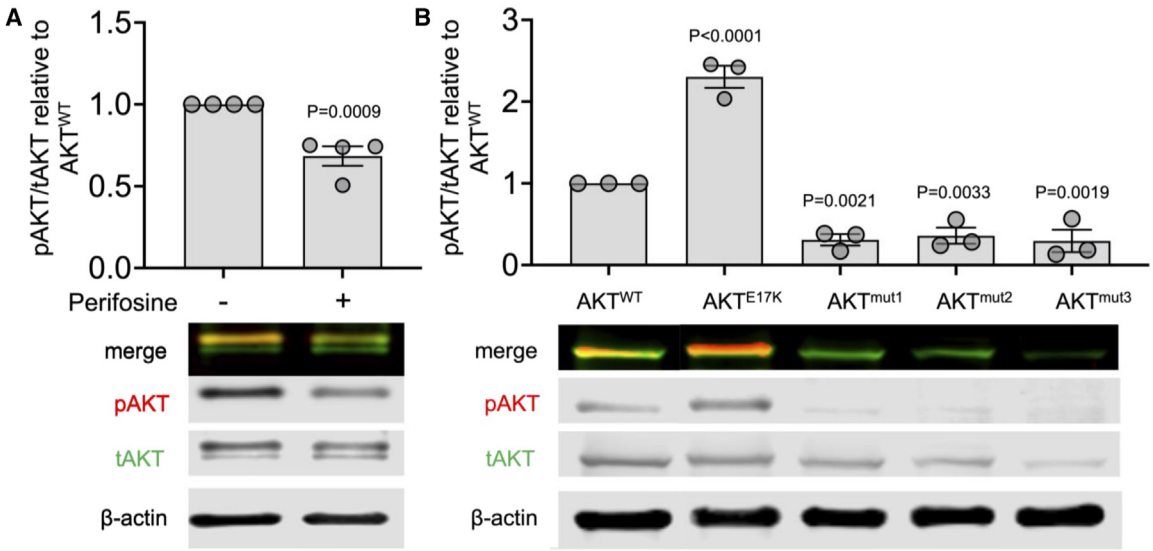

Figure 6. Mutations in the canonical and second binding sites attenuate AKT phosphorylation in untreated TNBC cells

(A) MDA-MB-468 cells were treated with VC and 20 μM of Perifosine. The pAKT/tAKT expression of EGFP-tagged AKT is shown on top, and representative immunoblots are shown below each plot. AKT phosphorylation of Perifosine treatment to the VC control was compared with one-tailed t test and $p \leq 0.05$ was considered significant.

(B) MDA-MB-468 cells were transfected with EGFP-tagged AKT^{WT}, AKT^{E17K} as a positive control and the AKT mutants (AKT^{mut1}, AKT^{mut2}, and AKT^{mut3}). The pAKT/tAKT expression of EGFP-tagged AKT for each transfection is shown on top and representative immunoblots are shown below each plot. Comparisons between the AKT phosphorylation of EGFP-tagged AKT^{WT} AKT^{E17K} positive control, and mutants were performed with one-way ANOVA with multiple comparisons. Data are presented as the mean of 3–4 independent replicates with SEM. See also Figure S15. Abbreviations: TNBC = triple-negative breast cancer, pAKT = phosphorylated AKT, tAKT = total AKT, VC = vehicle control.

previously known canonical and a second site) in the AKT-PH domain that are both required for the binding and orientation stabilization of AKT to the bilayer were identified. By targeting either binding site, or both sites in TNBC cells, AKT membrane localization and downstream functional activity significantly decreases and AKT re-distributes in the cytosol, where it is likely inactive. We have provided molecular insights into the first step of AKT activation and its interaction with PIP lipids to aid the direction for the control of this central oncogene in breast cancer.

It is important to mention some limitations of our study. Although phosphorylated AKT in the cytosol is short-lived, emerging data suggest evidence for nuclear PIPs and AKT signaling,[59] opening new avenues for AKT research. It would be crucial to study the mode of activation of nuclear AKT following nuclear PIP stimulation. Additionally, our *in vitro* validation was in TNBC cells; therefore, the role of the cooperative-binding sites of AKT still remain to be tested in other cancer types and upon various growth factor stimulation upstream AKT (IGF and, EGF). Our results suggest that the AKT-PH mutants bind PIP lipids with a non-productive state. Subsequently *in vitro*, the mutants localize in the cytosol, where AKT is likely inactive. A methodology limitation of our CG-MD simulation approach is that unbinding events and dissociation kinetics of WT and mutant AKT-PH/PIP interaction cannot be studied. Therefore, we cannot know for certain if the unavailability of PIP-binding residues in AKT-PH could rapidly dissociate the mutants from the membrane; however, we did show that the downstream functional activity of AKT is significantly reduced (Figure 6). Dephosphorylation kinetics in AKT have been previously studied with specialized techniques (live cell spectroscopy and fluorescence anisotropy), which could be applied to answer such questions in the future. While it would be good to get an estimate of the strength of the binding the PIP lipids in the two PIP binding sites, our current simulations do not allow us to give such an estimate. They do provide, however, a molecular model that explains in detail the AKT/PIP interaction and stabilization to the membrane. To estimate the affinity of PIPs to AKT PIP binding sites, one could perform free energy calculations; however, this was outside the scope of this study. Furthermore, even-though Martini 3 is now available, this work was done using Martini 2.1, for which a large body of work showed to be remarkably accurate[23,24,30,60–63] for peripheral membrane protein interactions. Moreover, while the underlying molecular details of phase separation of lipids, lipid-lipid interactions and the preference of PIPs for the L_o/L_d regions was not the main scope of this study, we note that our CG simulation model is a simplified model which lacks the asymmetrical nature of biological membranes. Symmetrical bilayers provide a simplified and controlled environment for understanding the dynamics of protein-lipid interactions. To address this limitation, we evaluated our computational predictions with lab-based studies; our computational models were in agreement to experimental data. In addition, it is important to note that although not the focus of this study, the cholesterol levels in cancer cell membranes are often altered,[13,64–66] and the exact distribution of cholesterol in membrane leaflets remains controversial,[67] due to methodological limitations and the fact that cholesterol has the ability to rapidly flip-flop between membrane leaflets. Advancements in methodologies like cryoelectron microscopy (cryo-EM)[68] could revolutionize the study of

lateral heterogeneities and lipid-lipid interactions (PIP/cholesterol-L_o domain interaction) in the cancer cells in the coming years.[69]

RESOURCE AVAILABILITY

Lead contact

Requests for further information and resources should be directed to and will be fulfilled by Dr James Thorne (j.l.thorne@leeds.ac.uk).

Materials availability

This study did not generate new unique reagents.

Data and code availability

MD simulation data have been deposited in doi: https://doi.org/10.5518/1313 and are publicly available. Information about the analysis of the data reported in this paper can be found in the STAR Methods section. This paper does not report original code. Any additional information required to reanalyze the data reported in this paper is available from the lead contact upon request.

ACKNOWLEDGMENTS

This work was funded by the Leeds Global Challenge Interdisciplinary Doctoral Scholarship. We thank Dr. Ruth Hughes from the Faculty of Biological Sciences Bioimaging facility for support with the Zeiss LSM 880 with Airyscan inverted confocal microscope, funded by the Wellcome Trust grant (WT104818MA). MD simulations were undertaken on ARC3 and ARC4, as part of the High-Performance Computing facilities at the University of Leeds, United Kingdom.

AUTHOR CONTRIBUTIONS

Conceptualization, J.L.T., A.C.K., S.D.C., A.I.I.T., and C.S.; methodology, C.S., J.L.T., and A.C.K.; formal analysis, C.S.; *in silico* investigation, C.S.; *in vitro* investigation, C.S. and M.X; resources, J.L.T. and A.C.K.; writing - original draft, C.S.; writing - review and editing, C.S., J.L.T., A.C.K., S.D.C., A.I.I.T, and M.X; visualisation, C.S.; supervision, J.L.T., A.C.K., S.D.C., and A.I.I.T.; project administration, J.L.T. and A.C.K.; funding acquisition, J.L.T., A.C.K., S.D.C., and A.I.I.T.

DECLARATION OF INTERESTS

The authors declare no competing interests.

STAR★METHODS

Detailed methods are provided in the online version of this paper and include the following:

- KEY RESOURCES TABLE
- EXPERIMENTAL MODEL AND STUDY PARTICIPANT DETAILS
  - Cell lines
- METHOD DETAILS
  - Coarse-grained molecular dynamic simulations
  - Atomistic molecular dynamic simulations
  - Molecular dynamics simulations analysis
  - Protein-lipid and lipid-lipid contacts
  - Protein-membrane z-axis distance and orientation
  - Density maps
  - Plasmid Construction and mutagenesis
  - DNA plasmid preparation
  - Plasmid transfections
  - Flow cytometry
  - Confocal microscopy
  - Protein extraction and quantification
  - Immunoblotting
- QUANTIFICATION AND STATISTICAL ANALYSIS

SUPPLEMENTAL INFORMATION

Supplemental information can be found online at https://doi.org/10.1016/j.str.2024.10.020.

Received: October 19, 2023
Revised: September 2, 2024
Accepted: October 10, 2024
Published: November 5, 2024

REFERENCES

1. Bellacosa, A., Kumar, C.C., Di Cristofano, A., and Testa, J.R. (2005). Activation of AKT kinases in cancer: implications for therapeutic targeting. Adv. Cancer Res. *94*, 29–86. https://doi.org/10.1016/S0065-230X(05)94002-5.
2. Noorolyai, S., Shajari, N., Baghbani, E., Sadreddini, S., and Baradaran, B. (2019). The relation between PI3K/AKT signalling pathway and cancer. Gene *698*, 120–128. https://doi.org/10.1016/j.gene.2019.02.076.
3. Fruman, D.A., Chiu, H., Hopkins, B.D., Bagrodia, S., Cantley, L.C., and Abraham, R.T. (2017). The PI3K Pathway in Human Disease. Cell *170*, 605–635. https://doi.org/10.1016/j.cell.2017.07.029.
4. Riggio, M., Perrone, M.C., Polo, M.L., Rodriguez, M.J., May, M., Abba, M., Lanari, C., and Novaro, V. (2017). AKT1 and AKT2 isoforms play distinct roles during breast cancer progression through the regulation of specific downstream proteins. Sci. Rep. *7*, 44244. https://doi.org/10.1038/srep44244.
5. Alessi, D.R., Deak, M., Casamayor, A., Caudwell, F.B., Morrice, N., Norman, D.G., Gaffney, P., Reese, C.B., MacDougall, C.N., Harbison, D., et al. (1997). 3-phosphoinositide-dependent protein kinase-1 (PDK1): structural and functional homology with the Drosophila DSTPK61 kinase. Curr. Biol. *7*, 776–789. https://doi.org/10.1016/S0960-9822(06)00336-8.
6. Sarbassov, D.D., Guertin, D.A., Ali, S.M., and Sabatini, D.M. (2005). Phosphorylation and regulation of Akt/PKB by the rictor-mTOR complex. Science *307*, 1098–1101. https://doi.org/10.1126/science.1106148.
7. Ebner, M., Lucic, I., Leonard, T.A., and Yudushkin, I. (2017). PI(3,4,5)P3 Engagement Restricts Akt Activity to Cellular Membranes. Mol. Cell *65*, 416–431. https://doi.org/10.1016/j.molcel.2016.12.028.
8. Truebestein, L., Hornegger, H., Anrather, D., Hartl, M., Fleming, K.D., Stariha, J.T.B., Pardon, E., Steyaert, J., Burke, J.E., and Leonard, T.A. (2021). Structure of autoinhibited Akt1 reveals mechanism of PIP3-mediated activation. Proc. Natl. Acad. Sci. USA *118*, e2101496118. https://doi.org/10.1073/pnas.2101496118.
9. Liu, S.L., Wang, Z.G., Hu, Y., Xin, Y., Singaram, I., Gorai, S., Zhou, X., Shim, Y., Min, J.H., Gong, L.W., et al. (2018). Quantitative Lipid Imaging Reveals a New Signaling Function of Phosphatidylinositol-3,4-Bisphophate: Isoform- and Site-Specific Activation of Akt. Mol. Cell *71*, 1092–1104.e5. https://doi.org/10.1016/j.molcel.2018.07.035.
10. Hanahan, D., and Weinberg, R.A. (2011). Hallmarks of cancer: the next generation. Cell *144*, 646–674. https://doi.org/10.1016/j.cell.2011.02.013.
11. Lučić, I., Rathinaswamy, M.K., Truebestein, L., Hamelin, D.J., Burke, J.E., and Leonard, T.A. (2018). Conformational sampling of membranes by Akt controls its activation and inactivation. Proc. Natl. Acad. Sci. USA *115*, E3940–E3949. https://doi.org/10.1073/pnas.1716109115.
12. Adam, R.M., Mukhopadhyay, N.K., Kim, J., Di Vizio, D., Cinar, B., Boucher, K., Solomon, K.R., and Freeman, M.R. (2007). Cholesterol sensitivity of endogenous and myristoylated Akt. Cancer Res. *67*, 6238–6246. https://doi.org/10.1158/0008-5472.CAN-07-0288.
13. Li, Y.C., Park, M.J., Ye, S.K., Kim, C.W., and Kim, Y.N. (2006). Elevated levels of cholesterol-rich lipid rafts in cancer cells are correlated with apoptosis sensitivity induced by cholesterol-depleting agents. Am. J. Pathol. *168*, 1107–1118. https://doi.org/10.2353/ajpath.2006.050959.
14. Lasserre, R., Guo, X.J., Conchonaud, F., Hamon, Y., Hawchar, O., Bernard, A.M., Soudja, S.M., Lenne, P.F., Rigneault, H., Olive, D., et al. (2008). Raft nanodomains contribute to Akt/PKB plasma membrane

recruitment and activation. Nat. Chem. Biol. *4*, 538–547. https://doi.org/10.1038/nchembio.103.

15. Levental, K.R., Surma, M.A., Skinkle, A.D., Lorent, J.H., Zhou, Y., Klose, C., Chang, J.T., Hancock, J.F., and Levental, I. (2017). omega-3 polyunsaturated fatty acids direct differentiation of the membrane phenotype in mesenchymal stem cells to potentiate osteogenesis. Sci. Adv. *3*, eaao1193. https://doi.org/10.1126/sciadv.aao1193.
16. Gao, X., Lowry, P.R., Zhou, X., Depry, C., Wei, Z., Wong, G.W., and Zhang, J. (2011). PI3K/Akt signaling requires spatial compartmentalization in plasma membrane microdomains. Proc. Natl. Acad. Sci. USA *108*, 14509–14514. https://doi.org/10.1073/pnas.1019386108.
17. Gao, X., and Zhang, J. (2008). Spatiotemporal analysis of differential Akt regulation in plasma membrane microdomains. Mol. Biol. Cell *19*, 4366–4373. https://doi.org/10.1091/mbc.E08-05-0449.
18. Berndt, N., Yang, H., Trinczek, B., Betzi, S., Zhang, Z., Wu, B., Lawrence, N.J., Pellecchia, M., Schönbrunn, E., Cheng, J.Q., and Sebti, S.M. (2010). The Akt activation inhibitor TCN-P inhibits Akt phosphorylation by binding to the PH domain of Akt and blocking its recruitment to the plasma membrane. Cell Death Differ. *17*, 1795–1804. https://doi.org/10.1038/cdd.2010.63.
19. Zhuang, L., Kim, J., Adam, R.M., Solomon, K.R., and Freeman, M.R. (2005). Cholesterol targeting alters lipid raft composition and cell survival in prostate cancer cells and xenografts. J. Clin. Invest. *115*, 959–968. https://doi.org/10.1172/JCI19935.
20. Rebecchi, M.J., and Scarlata, S. (1998). Pleckstrin homology domains: a common fold with diverse functions. Annu. Rev. Biophys. Biomol. Struct. *27*, 503–528. https://doi.org/10.1146/annurev.biophys.27.1.503.
21. Thomas, C.C., Deak, M., Alessi, D.R., and van Aalten, D.M.F. (2002). High-resolution structure of the pleckstrin homology domain of protein kinase B/Akt bound to phosphatidylinositol (3,4,5)-trisphosphate. Curr. Biol. *12*, 1256–1262. https://doi.org/10.1016/S0960-9822(02)00972-7.
22. Lemmon, M.A., Ferguson, K.M., and Schlessinger, J. (1996). PH domains: diverse sequences with a common fold recruit signaling molecules to the cell surface. Cell *85*, 621–624. https://doi.org/10.1016/s0092-8674(00)81022-3.
23. Yamamoto, E., Domański, J., Naughton, F.B., Best, R.B., Kalli, A.C., Stansfeld, P.J., and Sansom, M.S.P. (2020). Multiple lipid binding sites determine the affinity of PH domains for phosphoinositide-containing membranes. Sci. Adv. *6*, eaay5736. https://doi.org/10.1126/sciadv.aay5736.
24. Le Huray, K.I.P., Wang, H., Sobott, F., and Kalli, A.C. (2022). Systematic simulation of the interactions of pleckstrin homology domains with membranes. Sci. Adv. *8*, eabn6992. https://doi.org/10.1126/sciadv.abn6992.
25. Jian, X., Tang, W.K., Zhai, P., Roy, N.S., Luo, R., Gruschus, J.M., Yohe, M.E., Chen, P.W., Li, Y., Byrd, R.A., et al. (2015). Molecular Basis for Cooperative Binding of Anionic Phospholipids to the PH Domain of the Arf GAP ASAP1. Structure *23*, 1977–1988. https://doi.org/10.1016/j.str.2015.08.008.
26. Wang, Q., Vogan, E.M., Nocka, L.M., Rosen, C.E., Zorn, J.A., Harrison, S.C., and Kuriyan, J. (2015). Autoinhibition of Bruton's tyrosine kinase (Btk) and activation by soluble inositol hexakisphosphate. Elife *4*, e06074. https://doi.org/10.7554/eLife.06074.
27. Aleshin, A.E., Yao, Y., Iftikhar, A., Bobkov, A.A., Yu, J., Cadwell, G., Klein, M.G., Dong, C., Bankston, L.A., Liddington, R.C., et al. (2021). Structural basis for the association of PLEKHA7 with membrane-embedded phosphatidylinositol lipids. Structure *29*, 1029–1039.e3. https://doi.org/10.1016/j.str.2021.03.018.
28. Milburn, C.C., Deak, M., Kelly, S.M., Price, N.C., Alessi, D.R., and Van Aalten, D.M.F. (2003). Binding of phosphatidylinositol 3,4,5-trisphosphate to the pleckstrin homology domain of protein kinase B induces a conformational change. Biochem. J. *375*, 531–538. https://doi.org/10.1042/BJ20031229.
29. Agamasu, C., Ghanam, R.H., Xu, F., Sun, Y., Chen, Y., and Saad, J.S. (2017). The Interplay between Calmodulin and Membrane Interactions with the Pleckstrin Homology Domain of Akt. J. Biol. Chem. *292*, 251–263. https://doi.org/10.1074/jbc.M116.752816.
30. Yamamoto, E., Kalli, A.C., Yasuoka, K., and Sansom, M.S.P. (2016). Interactions of Pleckstrin Homology Domains with Membranes: Adding Back the Bilayer via High-Throughput Molecular Dynamics. Structure *24*, 1421–1431. https://doi.org/10.1016/j.str.2016.06.002.
31. Warfel, N.A., Niederst, M., and Newton, A.C. (2011). Disruption of the interface between the pleckstrin homology (PH) and kinase domains of Akt protein is sufficient for hydrophobic motif site phosphorylation in the absence of mTORC2. J. Biol. Chem. *286*, 39122–39129. https://doi.org/10.1074/jbc.M111.278747.
32. Parikh, C., Janakiraman, V., Wu, W.I., Foo, C.K., Kljavin, N.M., Chaudhuri, S., Stawiski, E., Lee, B., Lin, J., Li, H., et al. (2012). Disruption of PH-kinase domain interactions leads to oncogenic activation of AKT in human cancers. Proc. Natl. Acad. Sci. USA *109*, 19368–19373. https://doi.org/10.1073/pnas.1204384109.
33. Huang, J., and MacKerell, A.D., Jr. (2013). CHARMM36 all-atom additive protein force field: validation based on comparison to NMR data. J. Comput. Chem. *34*, 2135–2145. https://doi.org/10.1002/jcc.23354.
34. Lee, J., Cheng, X., Swails, J.M., Yeom, M.S., Eastman, P.K., Lemkul, J.A., Wei, S., Buckner, J., Jeong, J.C., Qi, Y., et al. (2016). CHARMM-GUI Input Generator for NAMD, GROMACS, AMBER, OpenMM, and CHARMM/OpenMM Simulations Using the CHARMM36 Additive Force Field. J. Chem. Theor. Comput. *12*, 405–413. https://doi.org/10.1021/acs.jctc.5b00935.
35. Carpten, J.D., Faber, A.L., Horn, C., Donoho, G.P., Briggs, S.L., Robbins, C.M., Hostetter, G., Boguslawski, S., Moses, T.Y., Savage, S., et al. (2007). A transforming mutation in the pleckstrin homology domain of AKT1 in cancer. Nature *448*, 439–444. https://doi.org/10.1038/nature05933.
36. Richardson, P.G., Eng, C., Kolesar, J., Hideshima, T., and Anderson, K.C. (2012). Perifosine , an oral, anti-cancer agent and inhibitor of the Akt pathway: mechanistic actions, pharmacodynamics, pharmacokinetics, and clinical activity. Expet Opin. Drug Metabol. Toxicol. *8*, 623–633. https://doi.org/10.1517/17425255.2012.681376.
37. Landgraf, K.E., Pilling, C., and Falke, J.J. (2008). Molecular mechanism of an oncogenic mutation that alters membrane targeting: Glu17Lys modifies the PIP lipid specificity of the AKT1 PH domain. Biochemistry *47*, 12260–12269. https://doi.org/10.1021/bi801683k.
38. Liu, Y., Lv, J.Y., Shi, J.F., Yang, M., Liu, S.H., Li, Z.W., Wang, H.B., Zhang, S.G., Liu, Z.W., Ding, J.B., et al. (2014). Targeting the raft-associated Akt signaling in hepatocellular carcinoma. BioMed Res. Int. *2014*, 836025. https://doi.org/10.1155/2014/836025.
39. Pommier, A.J.C., Alves, G., Viennois, E., Bernard, S., Communal, Y., Sion, B., Marceau, G., Damon, C., Mouzat, K., Caira, F., et al. (2010). Liver X Receptor activation downregulates AKT survival signaling in lipid rafts and induces apoptosis of prostate cancer cells. Oncogene *29*, 2712–2723. https://doi.org/10.1038/onc.2010.30.
40. Merezhko, M., Pakarinen, E., Uronen, R.L., and Huttunen, H.J. (2020). Live-cell monitoring of protein localization to membrane rafts using protein-fragment complementation. Biosci. Rep. *40*, BSR20191290. https://doi.org/10.1042/BSR20191290.
41. Hope, H.R., and Pike, L.J. (1996). Phosphoinositides and phosphoinositide-utilizing enzymes in detergent-insoluble lipid domains. Mol. Biol. Cell *7*, 843–851. https://doi.org/10.1091/mbc.7.6.843.
42. Pike, L.J., and Miller, J.M. (1998). Cholesterol depletion delocalizes phosphatidylinositol bisphosphate and inhibits hormone-stimulated phosphatidylinositol turnover. J. Biol. Chem. *273*, 22298–22304. https://doi.org/10.1074/jbc.273.35.22298.
43. Pike, L.J., and Casey, L. (1996). Localization and turnover of phosphatidylinositol 4,5-bisphosphate in caveolin-enriched membrane domains. J. Biol. Chem. *271*, 26453–26456. https://doi.org/10.1074/jbc.271.43.26453.
44. Hur, E.M., Park, Y.S., Lee, B.D., Jang, I.H., Kim, H.S., Kim, T.D., Suh, P.G., Ryu, S.H., and Kim, K.T. (2004). Sensitization of epidermal growth factor-induced signaling by bradykinin is mediated by c-Src. Implications for a

role of lipid microdomains. J. Biol. Chem. *279*, 5852–5860. https://doi.org/10.1074/jbc.M311687200.

45. Johnson, C.M., Chichili, G.R., and Rodgers, W. (2008). Compartmentalization of phosphatidylinositol 4,5-bisphosphate signaling evidenced using targeted phosphatases. J. Biol. Chem. *283*, 29920–29928. https://doi.org/10.1074/jbc.M805921200.
46. Myeong, J., Park, C.G., Suh, B.C., and Hille, B. (2021). Compartmentalization of phosphatidylinositol 4,5-bisphosphate metabolism into plasma membrane liquid-ordered/raft domains. Proc. Natl. Acad. Sci. USA *118*, e2025343118. https://doi.org/10.1073/pnas.2025343118.
47. Ceccarelli, D.F.J., Blasutig, I.M., Goudreault, M., Li, Z., Ruston, J., Pawson, T., and Sicheri, F. (2007). Non-canonical interaction of phosphoinositides with pleckstrin homology domains of Tiam1 and ArhGAP9. J. Biol. Chem. *282*, 13864–13874. https://doi.org/10.1074/jbc.M700505200.
48. Soubias, O., Pant, S., Heinrich, F., Zhang, Y., Roy, N.S., Li, J., Jian, X., Yohe, M.E., Randazzo, P.A., Lösche, M., et al. (2020). Membrane surface recognition by the ASAP1 PH domain and consequences for interactions with the small GTPase Arf1. Sci. Adv. *6*, eabd1882. https://doi.org/10.1126/sciadv.abd1882.
49. Calleja, V., Laguerre, M., Parker, P.J., and Larijani, B. (2009). Role of a novel PH-kinase domain interface in PKB/Akt regulation: structural mechanism for allosteric inhibition. PLoS Biol. *7*, e17. https://doi.org/10.1371/journal.pbio.1000017.
50. Bae, H., Viennet, T., Park, E., Chu, N., Salguero, A., Eck, M.J., Arthanari, H., and Cole, P.A. (2022). PH domain-mediated autoinhibition and oncogenic activation of Akt. Elife *11*, e80148. https://doi.org/10.7554/eLife.80148.
51. Baffi, T.R., Lordén, G., Wozniak, J.M., Feichtner, A., Yeung, W., Kornev, A.P., King, C.C., Del Rio, J.C., Limaye, A.J., Bogomolovas, J., et al. (2021). mTORC2 controls the activity of PKC and Akt by phosphorylating a conserved TOR interaction motif. Sci. Signal. *14*, eabe4509. https://doi.org/10.1126/scisignal.abe4509.
52. Cash, J.N., Chandan, N.R., Hsu, A.Y., Sharma, P.V., Deng, Q., Smrcka, A.V., and Tesmer, J.J.G. (2020). Discovery of Small Molecules That Target the Phosphatidylinositol (3,4,5) Trisphosphate (PIP3)-Dependent Rac Exchanger 1 (P-Rex1) PIP3-Binding Site and Inhibit P-Rex1-Dependent Functions in Neutrophils. Mol. Pharmacol. *97*, 226–236. https://doi.org/10.1124/mol.119.117556.
53. Nawrotek, A., Benabdi, S., Niyomchon, S., Kryszke, M.H., Ginestier, C., Cañeque, T., Tepshi, L., Mariani, A., St Onge, R.P., Giaever, G., et al. (2019). PH-domain-binding inhibitors of nucleotide exchange factor BRAG2 disrupt Arf GTPase signaling. Nat. Chem. Biol. *15*, 358–366. https://doi.org/10.1038/s41589-019-0228-3.
54. Jo, H., Lo, P.K., Li, Y., Loison, F., Green, S., Wang, J., Silberstein, L.E., Ye, K., Chen, H., and Luo, H.R. (2011). Deactivation of Akt by a small molecule inhibitor targeting pleckstrin homology domain and facilitating Akt ubiquitination. Proc. Natl. Acad. Sci. USA *108*, 6486–6491. https://doi.org/10.1073/pnas.1019062108.
55. Joh, E.H., Hollenbaugh, J.A., Kim, B., and Kim, D.H. (2012). Pleckstrin homology domain of Akt kinase: a proof of principle for highly specific and effective non-enzymatic anti-cancer target. PLoS One *7*, e50424. https://doi.org/10.1371/journal.pone.0050424.
56. Nierengarten, M.B. (2024). FDA approves capivasertib with fulvestrant for breast cancer. Cancer *130*, 835–836. https://doi.org/10.1002/cncr.35238.
57. Martorana, F., Motta, G., Pavone, G., Motta, L., Stella, S., Vitale, S.R., Manzella, L., and Vigneri, P. (2021). AKT Inhibitors: New Weapons in the Fight Against Breast Cancer? Front. Pharmacol. *12*, 662232. https://doi.org/10.3389/fphar.2021.662232.
58. Shaw, A.L., Parson, M.A.H., Truebestein, L., Jenkins, M.L., Leonard, T.A., and Burke, J.E. (2023). ATP-competitive and allosteric inhibitors induce differential conformational changes at the autoinhibitory interface of Akt1. Structure *31*, 343–354.e3. https://doi.org/10.1016/j.str.2023.01.007.
59. Zhou, X., Zhong, Y., Molinar-Inglis, O., Kunkel, M.T., Chen, M., Sun, T., Zhang, J., Shyy, J.Y.J., Trejo, J., Newton, A.C., and Zhang, J. (2020). Location-specific inhibition of Akt reveals regulation of mTORC1 activity in the nucleus. Nat. Commun. *11*, 6088. https://doi.org/10.1038/s41467-020-19937-w.
60. Borges-Araújo, L., Pereira, G.P., Valerio, M., and Souza, P.C.T. (2024). Assessing the Martini 3 protein model: A review of its path and potential. Biochim. Biophys. Acta, Proteins Proteomics *1872*, 141014. https://doi.org/10.1016/j.bbapap.2024.141014.
61. Corradi, V., Sejdiu, B.I., Mesa-Galloso, H., Abdizadeh, H., Noskov, S.Y., Marrink, S.J., and Tieleman, D.P. (2019). Emerging Diversity in Lipid-Protein Interactions. Chem. Rev. *119*, 5775–5848. https://doi.org/10.1021/acs.chemrev.8b00451.
62. Le Huray, K.I.P., Bunney, T.D., Pinotsis, N., Kalli, A.C., and Katan, M. (2022). Characterization of the membrane interactions of phospholipase Cgamma reveals key features of the active enzyme. Sci. Adv. *8*, eabp9688. https://doi.org/10.1126/sciadv.abp9688.
63. Atilgan, A.R., Durell, S.R., Jernigan, R.L., Demirel, M.C., Keskin, O., and Bahar, I. (2001). Anisotropy of fluctuation dynamics of proteins with an elastic network model. Biophys. J. *80*, 505–515. https://doi.org/10.1016/S0006-3495(01)76033-X.
64. Owen, D.M., Williamson, D.J., Magenau, A., and Gaus, K. (2012). Sub-resolution lipid domains exist in the plasma membrane and regulate protein diffusion and distribution. Nat. Commun. *3*, 1256. https://doi.org/10.1038/ncomms2273.
65. Kilin, V., Glushonkov, O., Herdly, L., Klymchenko, A., Richert, L., and Mely, Y. (2015). Fluorescence lifetime imaging of membrane lipid order with a ratiometric fluorescent probe. Biophys. J. *108*, 2521–2531. https://doi.org/10.1016/j.bpj.2015.04.003.
66. Levin-Gromiko, U., Koshelev, V., Kushnir, P., Fedida-Metula, S., Voronov, E., and Fishman, D. (2014). Amplified lipid rafts of malignant cells constitute a target for inhibition of aberrantly active NFAT and melanoma tumor growth by the aminobisphosphonate zoledronic acid. Carcinogenesis *35*, 2555–2566. https://doi.org/10.1093/carcin/bgu178.
67. Steck, T.L., and Lange, Y. (2018). Transverse distribution of plasma membrane bilayer cholesterol: Picking sides. Traffic *19*, 750–760. https://doi.org/10.1111/tra.12586.
68. Levental, I., Levental, K.R., and Heberle, F.A. (2020). Lipid Rafts: Controversies Resolved, Mysteries Remain. Trends Cell Biol. *30*, 341–353. https://doi.org/10.1016/j.tcb.2020.01.009.
69. Soteriou, C., Kalli, A.C., Connell, S.D., Tyler, A.I.I., and Thorne, J.L. (2021). Advances in understanding and in multi-disciplinary methodology used to assess lipid regulation of signalling cascades from the cancer cell plasma membrane. Prog. Lipid Res. *81*, 101080. https://doi.org/10.1016/j.plipres.2020.101080.
70. Abraham, M.J., Murtola, T., Schulz, R., Páll, S., Smith, J.C., Hess, B., and Lindahl, E. (2015). GROMACS: High performance molecular simulations through multi-level parallelism from laptops to supercomputers. SoftwareX *1–2*, 19–25.
71. Marrink, S.J., Risselada, H.J., Yefimov, S., Tieleman, D.P., and de Vries, A.H. (2007). The MARTINI force field: coarse grained model for biomolecular simulations. J. Phys. Chem. B *111*, 7812–7824. https://doi.org/10.1021/jp071097f.
72. Vance, J.E. (2015). Phospholipid synthesis and transport in mammalian cells. Traffic *16*, 1–18. https://doi.org/10.1111/tra.12230.
73. van Meer, G., Voelker, D.R., and Feigenson, G.W. (2008). Membrane lipids: where they are and how they behave. Nat. Rev. Mol. Cell Biol. *9*, 112–124. https://doi.org/10.1038/nrm2330.
74. Wen, Y., Vogt, V.M., and Feigenson, G.W. (2018). Multivalent Cation-Bridged PI(4,5)P(2) Clusters Form at Very Low Concentrations. Biophys. J. *114*, 2630–2639. https://doi.org/10.1016/j.bpj.2018.04.048.
75. Wang, H., Lo, W.T., Vujicic Zagar, A., Gulluni, F., Lehmann, M., Scapozza, L., Haucke, V., and Vadas, O. (2018). Autoregulation of Class II Alpha PI3K Activity by Its Lipid-Binding PX-C2 Domain Module. Mol. Cell *71*, 343–351.e4. https://doi.org/10.1016/j.molcel.2018.06.042.
76. Schöneberg, J., Lehmann, M., Ullrich, A., Posor, Y., Lo, W.T., Lichtner, G., Schmoranzer, J., Haucke, V., and Noe, F. (2017). Lipid-mediated PX-BAR

domain recruitment couples local membrane constriction to endocytic vesicle fission. Nat. Commun. *8*, 15873. https://doi.org/10.1038/ncomms15873.

77. Lolicato, F., Nickel, W., Haucke, V., and Ebner, M. (2024). Phosphoinositide switches in cell physiology - From molecular mechanisms to disease. J. Biol. Chem. *300*, 105757. https://doi.org/10.1016/j.jbc.2024.105757.

78. Wang, Q., Pechersky, Y., Sagawa, S., Pan, A.C., and Shaw, D.E. (2019). Structural mechanism for Bruton's tyrosine kinase activation at the cell membrane. Proc. Natl. Acad. Sci. USA *116*, 9390–9399. https://doi.org/10.1073/pnas.1819301116.

79. van den Bogaart, G., Meyenberg, K., Risselada, H.J., Amin, H., Willig, K.I., Hubrich, B.E., Dier, M., Hell, S.W., Grubmüller, H., Diederichsen, U., and Jahn, R. (2011). Membrane protein sequestering by ionic protein-lipid interactions. Nature *479*, 552–555. https://doi.org/10.1038/nature10545.

80. Wang, J., and Richards, D.A. (2012). Segregation of PIP2 and PIP3 into distinct nanoscale regions within the plasma membrane. Biol. Open *1*, 857–862. https://doi.org/10.1242/bio.20122071.

81. Fiser, A., and Sali, A. (2003). Modeller: generation and refinement of homology-based protein structure models. Methods Enzymol. *374*, 461–491. https://doi.org/10.1016/S0076-6879(03)74020-8.

82. Wassenaar, T.A., Ingólfsson, H.I., Böckmann, R.A., Tieleman, D.P., and Marrink, S.J. (2015). Computational Lipidomics with insane: A Versatile Tool for Generating Custom Membranes for Molecular Simulations. J. Chem. Theor. Comput. *11*, 2144–2155. https://doi.org/10.1021/acs.jctc.5b00209.

83. Hess, B. (2008). P-LINCS: A Parallel Linear Constraint Solver for Molecular Simulation. J. Chem. Theor. Comput. *4*, 116–122. https://doi.org/10.1021/ct700200b.

84. Wassenaar, T.A., Pluhackova, K., Böckmann, R.A., Marrink, S.J., and Tieleman, D.P. (2014). Going Backward: A Flexible Geometric Approach to Reverse Transformation from Coarse Grained to Atomistic Models. J. Chem. Theor. Comput. *10*, 676–690. https://doi.org/10.1021/ct400617g.

85. Jo, S., Kim, T., Iyer, V.G., and Im, W. (2008). CHARMM-GUI: a web-based graphical user interface for CHARMM. J. Comput. Chem. *29*, 1859–1865. https://doi.org/10.1002/jcc.20945.

86. Humphrey, W., Dalke, A., and Schulten, K. (1996). VMD: Visual Molecular Dynamics. J. Mol. Graph. *14*, 33–38.

STAR★METHODS

KEY RESOURCES TABLE

REAGENT or RESOURCE	SOURCE	IDENTIFIER
Antibodies		
AKT (pan) (40D4) mouse mAb	Cell Signalling Technology	Cat#2920; RRID:AB_1147620
Phospho-Akt (Ser473) (193H12) Rabbit mAb	Cell Signalling Technology	Cat#4058; RRID:AB_331168
β-Actin (8H10D10) Mouse mAb	Cell Signalling Technology	Cat#3700; RRID:AB_2242334
IRDye 800CV goat anti-mouse	Cell Signalling Technology	Cat#926-68170; RRID:AB_10956589
IRDye 680RD goat anti-rabbit	LI-COR Biosciences	Cat#926-68071; RRID:AB_10956166
Bacterial and virus strains		
E.coli DH10B competent cells	Invitrogen	Cat#1296606; N/A
Chemicals, peptides, and recombinant proteins		
ampicillin	Sigma–Aldrich	Cat#A9518; N/A
Lipofectamine 3000	Thermo Fisher	Cat#L3000015; N/A
ProLong Diamond Antifade Mountant with DAPI	Thermo Fisher	Cat#17625062; N/A
HALT™ Protease & Phosphatase Inhibitor Cocktail (100x)	Thermo Fisher	Cat#861281; N/A
NUPAGE lithium dodecyl sulfate (LDS sample loading buffer	Thermo Fisher	Cat#NP0007; N/A
dithiothreitol (DTT) reducing agent	Thermo Fisher	Cat#NP0004; N/A
methanol-activated polyvinylidene fluoride (PVDF) membrane	Merck	Cat#IPFL00010; N/A
tris-buffered saline (TBS) Odyssey Blocking Buffer	LI-COR Biosciences	Cat#92750000; N/A
Perifosine	Sigma-Aldrich	Cat#SML0612; N/A
Critical commercial assays		
HiSpeed Plasmid Maxi Kit	Qiagen	Cat#12663; N/A
Pierce™ BCA Protein Assay Kit	Thermo Fisher	Cat#23227; N/A
Deposited data		
Molecular dynamics simulation trajectories	This paper	https://doi.org/10.5518/1313
High resolution structure of AKT-PH	Milburn et al.	PDB: 1UNQ
Experimental models: Cell lines		
MDA-MB-468	ATCC	RRID: CVCL_0419
Recombinant DNA		
Plasmid: AKT^{WT}-mCherry (See Table S1)	This paper	N/A
Plasmid: AKT^{WT}-EGFP (See Table S1)	This paper	N/A
Plasmid: AKT^{E17K}-EGFP (See Table S1)	This paper	N/A
Plasmid: AKT^{mut1}-EGFP (See Table S1)	This paper	N/A
Plasmid: AKT^{mut2}-EGFP (See Table S1)	This paper	N/A
Plasmid: AKT^{mut3}-EGFP (See Table S1)	This paper	N/A
Plasmid: AKT-PH^{mut3}-mCherry (See Table S1)	This paper	N/A
pcDNA3.1 empty vector (See Table S1)	Gifted by Dr. Thomas Hughes, University of Leeds	Addgene plasmid # 40728; RRID: Addgene_40728
HA-GFP reporter (See Table S1)	Gifted by Dr. Thomas Hughes, University of Leeds	N/A

(*Continued on next page*)

Continued

REAGENT or RESOURCE	SOURCE	IDENTIFIER
Software and algorithms		
GROMACS 5.0.7	Abraham et al.[70]	www.gromacs.org
MODELLER	Fiser et al.[81]	N/A
CHARRM-Gui	Jo et al.[85]; Lee et al.[34]	www.charmm-gui.org
Visual Molecular Dynamics (VMD)	Humphrey et al.[86]	https://www.ks.uiuc.edu/Research/vmd/
XmGrace	Weizmann Institute of Science	https://plasma-gate.weizmann.ac.il/Grace
GraphPad Prism v9	GraphPad Software Inc	https://www.graphpad.com
Python version 3	Python Software Foundation	https://www.python.org
Image Studio™ Lite	LI-COR Biosciences	https://www.licor.com/bio/image-studio/
Other		
UNIPROT	EMBL-EBI, Swiss Institute of Bioinformatics (SIB), and Protein Information Resources (PIR)	https://www.uniprot.org

EXPERIMENTAL MODEL AND STUDY PARTICIPANT DETAILS

Cell lines

The MDA-MB-468 (triple-negative breast cancer) cell line were originally obtained from ATCC (Manassas, USA, RRID: CVCL_0419) and were routinely cultured in Dulbecco's modified Eagle's medium (DMEM) GlutaMax (Thermo Fisher, UK, Cat#31966047) supplemented with 10% fetal bovine serum (FBS) (Thermo Fisher, UK, Cat#11560636). Cells were maintained in a humidified incubator (Panasonic, MCO-170A1CUV-PE, UK) at 37°C in a 5% CO_2 air environment. Cells were routinely passaged at 80% confluence and re-plated at $1x10^6$ in 75 cm^2 (T75) tissue culture flasks (Thermo Fisher Scientific, UK, Cat#10364131). To subculture, the media was removed from the cells, and 5 ml of Dulbecco's phosphate-buffered saline (DPBS) (Thermo Fisher, UK, Cat#10209252) was used to wash any residual culture media away. Trypsin-EDTA (x10) (Thermo Fischer, UK, Cat#10779413) was diluted to a ratio of 1:10 with PBS and 3 ml was used to detach cells from flasks through incubation of 3-5 min at 37°C. After cell detachment from the cell culture flask, 7 ml FBS-containing DMEM was added to deactivate trypsin. In order to count the cells, 10 μl of cell suspension was added to the hemocytometer with 10 μl of trypan blue (Thermo Fisher, UK, Cat#15250061) to identify live and dead cells. Cells were then centrifuged at 1200 rpm for 5 min, and the appropriate volume of FBS-containing DMEM was added to the cell pellets to reach the concentration of $1x10^6$ cells/mL.

METHOD DETAILS

Coarse-grained molecular dynamic simulations

Coarse-grained molecular dynamics (CG-MD) simulations with AKT-PH were performed using GROMACS 5.0.7[70] with the Martini 2.1 force field.[71] A high-resolution (0.98 Å) crystal structure of AKT-PH (Protein Data Bank (PDB): 1UNQ)[28] was placed at a ~7 nm z-axis distance from a symmetric model membrane. The lipid components of the membrane were as follows: DPPC 37%, DLiPC 25%, CHOL 28%, PIP_2 5% and PIP_3 5% (mol%). A concentration of 10% of PIP lipids was chosen for this study. Whilst lipidomic studies indicate that the global concentration of PIP lipids in membranes is less than 5%,[72,73] it's important to note that the local concentration can be substantially higher via nanoscale localisation of PIPs and their association with specific proteins.[74] For example, during signalling, positively charged patches in AKT can attract up to 5 PIPs, as seen in silico[23,24] and experimentally[29] in AKT studies with different model membrane composition to here. As a result, it is believed that this could result in much higher concentrations of even rare PIP species at defined intracellular sites, as previously observed[75–77] with a local PIP concentration reaching way above 10% (from 20% up to 82% in protein microdomains).[78–80] Additionally, a computational study of AKT, which tested both 4% and 10% of PIP lipids in their membrane composition, showed that the PIP concentration did not bias their observations of PIP clustering, however clustering and PIP binding did take longer to occur.[24] This holds true in our system, as when the lipid-contact analysis is performed in a system with 5% PIP lipids, we still observe the canonical and second binding site (Figure S11). Unresolved atoms or residues in the PH domains were compared to the WT UniProt sequence and were modelled using MODELLER.[81] In silico mutations in the PH domain were also modelled using MODELLER.[81] The processed PH domain PDB structure was converted to a CG representation using the *martinize* tool that is provided by the Martini developers[71] and was placed into a 13.5 nm x 13.5 nm x 22 nm simulation box (X, Y, Z dimensions). The insane tool was used to add ions, solvent water and symmetric membrane bilayers at a z distance of ~7 nm from the protein.[82] The systems were solvated with ~26000 CG-water molecules and neutralised with Na+ Cl- ions at 0.15 M. In order to model the secondary and tertiary structure, an elastic network model was applied to all protein backbone particles with a cut-off distance of 0.7 nm and a force constant of 1000 kJ mol^{-1} nm^{-1} as used in other CG-MD simulations involving PH-containing peripheral proteins.[23,24,30,62,63]

Systems were energy minimised for 5000 steps using the steepest descent method. Systems were then equilibrated for 5 ns with the protein backbone position-restrained. Equilibration and production simulations were conducted using an NPT ensemble. The velocity-rescaling thermostat was used to maintain a temperature of 298 K with a coupling time of 1 ps. The Parrinello-Rahman barostat (semi-isotropic conditions) was used to maintain the pressure of 1 bar using a 12 ps coupling time. The LINCS algorithm was used to constrain bond lengths.[83] The final snapshot from the equilibrated simulation was used to generate 20 independent seeds for production simulations (per system). For each system, 20 x 7 μs repeat CG systems with 20 fs time step were simulated, initiated from the equilibrated system, with random velocities.

Atomistic molecular dynamic simulations

The final frame of the one of the CG simulation repeat was backmapped to an atomistic (AT) representation. The backward method[71] was used to backmap the system from the Martini to the CHARMM36 force field.[34,84,85] The backmapped system was energy minimized and was subject to 5 ns of equilibration with the protein backbone restrained. The production simulation was run for 100 ns, with a 2 fs timestep, at 298 K and semi-isotropic Parinello-Rahman pressure coupling at 1 bar, as previously described.[24]

Molecular dynamics simulations analysis

CG-MD simulations were analysed using Gromacs 5.0.7.[70] Visualisation and rendering were performed with Visual Molecular Dynamics (VMD),[86] XmGrace (https://plasma-gate.weizmann.ac.il/Grace/) and GraphPad Prism 9 (GraphPad Software Inc, USA) were used for plotting. Convergence analysis was carried out using different-sized simulation replicate samples (n of 5, 10, 15 and 20) and can be found in Figure S12.

Protein-lipid and lipid-lipid contacts

In order to calculate the z-axis distance between the centre of mass of the protein and the centre of mass of the membrane over time, the *gmx dist* command was used.[70] The cut-off for membrane binding was set at 4.3 nm z-axis, and the cut-off for protein orientation stabilisation was set at 3.6 nm z-axis. These cut-offs were chosen based on z-distances, which showed that when the centre of mass of the protein and the centre of mass of the membrane was set at 4.3 nm or less the protein interacted to the lipids of the bilayer. The orientation stabilisation cut-off of 3.6 nm was selected as at this z-distance the protein showed no change in its orientation through time, lipid interactions occurred consistently with the same AKT-PH residues and remained bound to the bilayer until the end of the 7 μs, indicating a stabilised orientation.

The contacts between protein residues and lipids particles (PIP_2 and PIP_3 headgroups) were analysed using the gromacs *gmx mindist* command[70] and in-house python scripts. A 0.55 nm and 0.40 nm distance cut-off were used to define a contact for CG and atomistic simulations, respectively. For contact analysis of WT protein, contacts were normalised by dividing the total amount of contacts at each residue by the total contacts made by the residue with the highest number of contacts within that lipid group (total contact number of each residue/ total contacts by residue with highest contacts). Therefore, the residue with the highest number of contacts had the normalised value of 1, with all other contacts normalised relative to that residue. For comparison of WT protein compared to mutants, normalisation was also done by dividing the number of PIP contacts of each residue by the number of PIP molecules and the total number of frames analysed. For the CG simulations normalised contacts were presented as averages of 20 simulation repeats per system, and residues with contacts above 70% were considered key contributions to PIP interactions. For the atomistic simulations normalised contacts were presented as averages of 3 simulation repeats per system, and residues with contacts above 70% were considered key contributions to PIP interactions. An upper cut-off of 80% was also presented, which indicates the most important residues for electrostatic interaction with PIPs in the higher-resolution atomistic system. The RMSD over time and RMSF per residue of protein backbone particles were performed using the *gmx rms* and *gmx rmsf* commands.[70]

In order to calculate the number of PIP lipids closely associated with the protein in the CG systems (PIP clustering) or lipid-lipid contacts during the simulation time, the *gmx mindist*[70] command was used. Specifically, the CG phosphate bead (connecting the tail and the headgroup) of PIPs within a 0.6 nm distance of the protein or other lipids were considered contacts. Protein was selected as a group; therefore, a contact of a specific lipid with multiple protein residues was counted as 1 contact instead of multiple contacts. A larger cut-off distance of 0.6 nm was selected for this analysis (than the analysis above) due to the increased distance between the connecting phosphate and the headgroup phosphates. Contacts were presented as averages of 20 simulation repeats per system ±SD.

Protein-membrane z-axis distance and orientation

Analysis of protein orientation was performed using the *gmx gangle*[70] command to measure the angle theta between the plane defined by three residues in AKT-PH (94, 102 and 108, in structured regions of the protein) and the z-axis of the simulation box, as previously described[62] (Figure S5). Using an in-house python script,[62] the measurements were corrected to account for the periodic boundary conditions, which allowed the protein to travel through the periodic boundary on the z-axis and bind either leaflet on the membrane.

Then, to generate two-dimensional histograms showing the populations of the protein's preferred orientation (from all 20 simulation repeats) when unbound or bound to the membrane, z-distance-orientation (theta) plots were generated over all simulation frames. Normalisation was performed by dividing with the maximum of all densities. One-dimensional histograms were also generated to show the orientation states when the membrane z-axis distance was less than 4.3 nm, representing all protein-bound membrane

states or less than 3.6 nm to show only the stabilised orientation protein states. Convergence analysis was carried out using different-sized simulation replicate samples (n of 5, 10, 15 and 20) and can be found in Figure S12.

Density maps

In order to generate two-dimensional density maps of the protein and individual lipid species around the protein, the trajectories of all simulation repeats per system were concatenated with *gmx trjcat,*[70] and the protein orientation was fitted using *gmx trjconv.* In order to produce two-dimensional number-density maps of proteins and lipids in the x-y plane, with summation of density along the *z*-axis, *gmx densmap* and *gmx xpm2ps* commands were used.[70]

Plasmid Construction and mutagenesis

Construction of clonal genes and the expression vector were performed at Twist Bioscience (San Francisco, USA). WT and mutated forms of the human *AKT1* were fused with green fluorescent protein (EGFP) or red fluorescent protein (mCherry) in the C-terminus and cloned into the pTwist CMV Puro expression vector. Sequences were NGS sequence verified by Twist Bioscience to confirm the presence of the requested sequences (Table S1).

DNA plasmid preparation

The plasmid DNA samples were transformed into E.coli DH10B competent cells (Invitrogen, UK, Cat#1296606), and 50 μg/ml ampicillin (Sigma–Aldrich, UK, Cat#A9518) supplemented Lysogeny Broth (LB) cultures of plasmid was grown. The plasmid DNA was purified using a HiSpeed Plasmid Maxi Kit (Qiagen, Germany Cat#12663) according to the manufacturer's instructions. The purified plasmids' concentration and purity (based on 260/280 nm optical density) were determined with a NanoDrop Spectrophotometer (Thermofisher, UK).

Plasmid transfections

AKT mutants (Red or Green) were then co-transfected with AKT^{WT} of reciprocal colour into triple-negative breast cancer (TNBC). Transient transfections were performed in 6-well plates using Lipofectamine 3000 (Thermo Fisher Scientific, UK, Cat#L3000015), according to the manufacturer's guidelines. For protein expression analysis, a starting cell number of $4x10^5$ MDA-MB-468 cells were seeded onto 6-well plates and incubated overnight. 24 h after seeding, the transfection complexes were diluted in OptiMEM (Thermo Fischer, UK, Cat#31985062) with Lipofectamine. For the immunofluorescence co-transfection experiments, 800 ng of pcDNA3.1 empty vector (gift from Dr. Thomas Hughes, University of Leeds) was used as a carrier for 100 ng of EGFP-fused AKT and 100 ng of mCherry-fused AKT plasmid mixed in OptiMEM (Thermo Fischer, UK, Cat#31985062) with Lipofectamine 3000 (Thermo Fisher Scientific, UK, Cat#L3000015) at 7.5:1 ratio. For the immunoblotting experiments, 900 ng of pcDNA3.1 empty vector was used as a carrier for 200 ng of EGFP-fused AKT. The amount of each reporter was corrected for its size in base pairs relative to the HA-GFP reporter control (gift from Dr. Thomas Hughes, University of Leeds) to ensure equimolar amounts of each plasmid were transfected. The transfection complexes were incubated with cells for 20 h, and then the media was removed and changed with fresh FBS-containing DMEM. 48 h post-transfection, transfected cells were checked with a fluorescent microscope (Ceti, Medicine, UK), and cells were prepared for flow cytometry and confocal microscopy. Transfection efficiency can be found in Figure S13.

Flow cytometry

Flow cytometry was used to measure transfection efficiency. 48 h post-transfections, cells were washed with 1ml of PBS and were trypsinised (500 μL) for 5 min at 37°C to be detached. 1 ml of FBS-containing DMEM was added, and cells were transferred to 25 ml falcon tubes and were centrifuged at 1.2 rpm for 5 min. Finally, the supernatant was discarded, and pellets were resuspended in 1 ml of ice-cold PBS in 1.5 ml eppendorf tubes. Cell suspensions were kept in the dark on ice and were immediately analysed for flow cytometry using a CytoFLEX S (Beckman Coulter, UK). At least 10 000 events were measured for each sample. MDA-MB-468 cells were gated to exclude cellular debris and doublets using side scatter (SSC) area versus height plot (SSC-A/SSC-H). The population of single cells was then plotted on an EGFP vs mCherry plot, and quadrant gates were added to determine EGFP and mCherry positive cells.

Confocal microscopy

Transfected cells seeded onto 22 x 22 mm ethanol sterilised coverslips (VWR International, UK, Cat#631-0125) in 6-well plates were prepared for confocal microscopy 48 h post-transfection. The cells were washed 2x with PBS and immediately fixed with 1 ml of 10 % neutral buffered formalin (Sigma-Aldrich UK, Cat#F5554-4L) for 15 min at room temperature. Cells were then washed 4x with PBS, and coverslips were mounted onto SuperFrost Plus slides with one drop of ProLong Diamond Antifade Mountant with DAPI (Thermo Fisher Scientific, UK, Cat#17625062). Before confocal imaging, the slides were left to cure for 24 h at 4°C. Confocal images were at the Bio-imaging and Flow Cytometry Facility in the Faculty of Biological Sciences, University of Leeds, using Zen-Imaging software (Zeiss, UK) on an LSM 880 with Airyscan (Zeiss, UK), equipped with a 40x Plan-Apochromat 1.4 oil immersion objective (Zeiss, UK). DAPI, EGFP and mCherry were excited with the 405 nm, 488 nm and 561 nm laser lines, respectively. Evidence for the absence of crossover of fluorescence emission and EGFP/mCherry spectral overlap of EGFP can be found in Figure S14. For each sample, 3 x 3 TileScan images at two different fields of cells were imaged along with 1-2 zoomed confocal images per sample. All samples were blind-labelled and were unknown to the microscopist. A two-colour system was employed for qualitative analysis to allow

simultaneous imaging of WT and mutant proteins in the same cell. All double-transfected cells in each field of view were included in the analysis for each sample. The line profile function in Fiji macOS (LOCI, USA) was used for calculating the relative ratio between EGFP and mCherry intensity at the plasma membrane and cytosol. Briefly, a line was drawn across the cell image and over the non-nuclear region, and the distance-dependent intensity plot with two peaks indicating the plasma membrane was obtained. The average of the two intensity peaks for the plasma membrane and the cytosol were calculated for the same distances of EGFP and mCherry channel intensity. Three lines were at least drawn for each cell, and the values were averaged. The mean mCherry or EGFP membrane to cytosol fluorescence intensity ratio (MCFR) was calculated by Equation 1.

$$MCFR \frac{membrane\ fluorescence\ intensity}{cytosol\ fluorescence\ intensity + membrane\ fluorescence\ intensity} \quad \text{(Equation 1)}$$

Protein extraction and quantification

Cells were washed with PBS prior to lysis with radioimmunoprecipitation assay (RIPA) buffer [10 mM Tris hydrogen chloride (Tris-HCL) pH 8, 140 mM sodium chloride (NaCl), 0.1% sodium dodecyl-sulfate (SDS), 1% Triton X-100, 0.1% sodium deoxycholate, 1 mM ethylenediaminetetraacetic acid (EDTA), 0.5 mM ethylene glycol tetraacetic acid (EGTA), supplemented with HALT™ Protease & Phosphatase Inhibitor Cocktail (100x) (Thermo Fisher, UK, Cat#861281)] that was added freshly prior each experiment. The lysed pellets were incubated on ice for 15 min and centrifuged for 10 min at 11500 g, 4°C. Protein concentration was quantified using the Pierce™ BCA Protein Assay Kit (Thermo Fisher, UK, Cat#23227), following the manufacturer's instructions. A standard curve was produced using bovine serum albumin (BSA) serially diluted in RIPA from 0-200 μg/mL. Proteins samples were diluted 1/10 in RIPA and measured using CLARIOstar plate reader (BMG LABTECH, Germany) at an absorbance of 562 nm. Lysates were kept at -80°C.

Immunoblotting

Thirty-five micrograms of protein lysate were combined with NUPAGE lithium dodecyl sulfate (LDS sample loading buffer (Thermo Fisher, UK, Cat#NP0007) and dithiothreitol (DTT) reducing agent (Thermo Fisher, UK, Cat#NP0004) and were heated for 10 min at 70°C. The denatured protein lysates were loaded onto a 12% SDS gel and electrophoresed at 80 V for one hour and then at a constant of 120 V and run until the loading dye front reached the bottom of the gel. Following electrophoresis, the protein samples were transferred onto a methanol-activated polyvinylidene fluoride (PVDF) membrane (Merck, UK, Cat#IPFL00010). The membrane was blocked with tris-buffered saline (TBS) Odyssey Blocking Buffer (LI-COR Biosciences, UK, Cat#92750000) for 1h. Proteins were probed with antibodies specific to total AKT (tAKT, [Cell Signalling Technology, UK, Cat#2920; RRID:AB_1147620, dilution 1/500]), phosphorylated AKT residue (Cell Signalling Technology, UK, Cat#4058; RRID:AB_331168, pAKT, [dilution 1/1000]) and beta-actin (Cell Signalling Technology, UK, Cat#3700; RRID:AB_2242334, β-actin [dilution 1/10000]) overnight at 4°C on a shaking incubator. The membranes were blocked with TBS-T and TBS and probed with LI-COR goat anti-mouse (Cat#9268170; RRID: AB_10956589) and goat anti-rabbit secondary (Cat#926-68071; RRID: 10956166) antibodies mouse (dilution 1/15000) for 1h at 25°C and the signal was visualised with Odyssey CLx Imaging System (LI-COR, Biosciences, UK). Densitometry analysis was performed with Image Studio Lite Acquisition Software (LI-COR Biosciences, UK, Version 5.2.5). The AKT inhibitor Perifosine (20μM, Sigma-Aldrich UK, Cat#SML0612) was used as a negative control treatment and was solubilised in sterile distilled water. The EGFP-tagged AKT constructs were differentiated from endogenous AKT due to their size difference of 26 kDa, with endogenous AKT being 60 kDa and EGFP-tagged AKT being around 86 kDa. Densitometry values of phosphorylated EGFP-tagged AKT were normalised to total EGFP-tagged AKT. Raw immunoblot images can for every biological replicate can be found in Figure S15.

QUANTIFICATION AND STATISTICAL ANALYSIS

Statistical analysis was performed using GraphPad Prism 9 (GraphPad Software Inc, USA). Comparison between the membrane and cytosol intensity ratio of mCherry-fused WT AKT was determined by a two-tailed unpaired t-test. A quantitative nested t-test analysis showing the biological and technical replicates (multiple cells per confocal image) was performed in GraphPad Prism to compare the membrane to cytosol ratio of AKT localisation between WT and mutant AKT. Comparisons between mCherry and EGFP intensities of different co-transfection experiments were determined using one-way ANOVA with Holm Sidak's multiple comparisons test. Transfection efficiency of co-transfections of mutated AKTs (fused to EGFP) and WT AKT (fused to mCherry) compared to WT double transfection (AKT^{WT}-mCherry & AKT^{WT}-EGFP) were determined with a one-way ANOVA with Holm-Sidak correction for multiple testing. Comparisons between the AKT phosphorylation of EGFP-tagged AKT^{WT} and mutants were performed with one-way ANOVA with multiple comparisons. Perifosine treatment to the vehicle control were compared with one-tailed unpaired t-test. A P-value of ≤ 0.05 was considered significant.